Physics of Plasmas

RESEARCH ARTICLE | MAY 02 2024

Review of the second charged-particle transport coefficient code comparison workshop

Special Collection: Charged-Particle Transport in High Energy Density Plasmas

Lucas J. Stanek ; Alina Kononov ; Stephanie B. Hansen ; Brian M. Haines ; S. X. Hu ; Patrick F. Knapp ; Michael S. Murillo ; Liam G. Stanton ; Heather D. Whitley ; Scott D. Baalrud ; Lucas J. Babati ; Andrew D. Baczewski ; Mandy Bethkenhagen ; Augustin Blanchet ; Raymond C. Clay, III ; Kyle R. Cochrane ; Lee A. Collins ; Amanda Dumi ; Gerald Faussurier ; Martin French ; Zachary A. Johnson ; Valentin V. Karasiev ; Shashikant Kumar ; Meghan K. Lentz ; Cody A. Melton ; Katarina A. Nichols ; George M. Petrov ; Vanina Recoules ; Ronald Redmer ; Gerd Röpke ; Maximilian Schörner ; Nathaniel R. Shaffer ; Vidushi Sharma ; Luciano G. Silvestri ; François Soubiran ; Phanish Suryanarayana ; Mikael Tacu ; Joshua P. Townsend ; Alexander J. White

Phys. Plasmas 31, 052104 (2024)
https://doi.org/10.1063/5.0198155

Review of the second charged-particle transport coefficient code comparison workshop

Cite as: Phys. Plasmas **31**, 052104 (2024); doi: 10.1063/5.0198155
Submitted: 16 January 2024 · Accepted: 9 April 2024 ·
Published Online: 2 May 2024

View Online Export Citation CrossMark

Lucas J. Stanek,[1,a)] Alina Kononov,[1] Stephanie B. Hansen,[1,b)] Brian M. Haines,[2] S. X. Hu,[3] Patrick F. Knapp,[2] Michael S. Murillo,[4] Liam G. Stanton,[5] Heather D. Whitley,[6] Scott D. Baalrud,[7] Lucas J. Babati,[7] Andrew D. Baczewski,[1] Mandy Bethkenhagen,[8] Augustin Blanchet,[9,10] Raymond C. Clay III,[1] Kyle R. Cochrane,[1] Lee A. Collins,[2] Amanda Dumi,[1] Gerald Faussurier,[9] Martin French,[11] Zachary A. Johnson,[4] Valentin V. Karasiev,[3] Shashikant Kumar,[12] Meghan K. Lentz,[1] Cody A. Melton,[1] Katarina A. Nichols,[3] George M. Petrov,[13] Vanina Recoules,[9,10] Ronald Redmer,[11] Gerd Röpke,[11] Maximilian Schörner,[11] Nathaniel R. Shaffer,[3] Vidushi Sharma,[2] Luciano G. Silvestri,[4] François Soubiran,[9,10] Phanish Suryanarayana,[12,14] Mikael Tacu,[9,10] Joshua P. Townsend,[1] and Alexander J. White[2]

AFFILIATIONS

[1]Sandia National Laboratories, Albuquerque, New Mexico 87123, USA
[2]Los Alamos National Laboratory, Los Alamos, New Mexico 87545, USA
[3]Laboratory for Laser Energetics, University of Rochester, Rochester, New York 14623, USA
[4]Department of Computational Mathematics, Science and Engineering, Michigan State University, East Lansing, Michigan 48824, USA
[5]Department of Mathematics and Statistics, San José State University, San José, California 95192, USA
[6]Lawrence Livermore National Laboratory, Livermore, California 94550, USA
[7]Department of Nuclear Engineering and Radiological Sciences, University of Michigan, Ann Arbor, Michigan 48109, USA
[8]LULI, CNRS, CEA, Sorbonne Université, Ecole Polytechnique - Institut Polytechnique de Paris, 91128 Palaiseau, France
[9]CEA-DAM-DIF, F-91297 Arpajon, France
[10]Université Paris-Saclay, CEA, Laboratoire Matière sous conditions extrêmes, 91680 Bruyères-le-Châtel, France
[11]Institut für Physik, Universität Rostock, D-18051 Rostock, Germany
[12]College of Engineering, Georgia Institute of Technology, Atlanta, Georgia 30332, USA
[13]Naval Research Laboratory, Plasma Physics Division, Washington, District of Columbia 20375, USA
[14]College of Computing, Georgia Institute of Technology, Atlanta, Georgia 30332, USA

Note: This paper is part of the Special Topic: Charged-Particle Transport in High Energy Density Plasmas.
[a)]**Author to whom correspondence should be addressed:** lstanek@sandia.gov
[b)]**Electronic mail:** sbhanse@sandia.gov

ABSTRACT

We report the results of the second charged-particle transport coefficient code comparison workshop, which was held in Livermore, California on 24–27 July 2023. This workshop gathered theoretical, computational, and experimental scientists to assess the state of computational and experimental techniques for understanding charged-particle transport coefficients relevant to high-energy-density plasma science. Data for electronic and ionic transport coefficients, namely, the direct current electrical conductivity, electron thermal conductivity, ion shear viscosity, and ion thermal conductivity were computed and compared for multiple plasma conditions. Additional comparisons were carried out for electron–ion properties such as the electron–ion equilibration time and alpha particle stopping power. Overall, 39 participants submitted calculated results from 18 independent approaches, spanning methods from parameterized semi-empirical models to time-dependent density functional theory. In the cases studied here, we find significant differences—several orders of magnitude—between approaches, particularly at lower temperatures, and smaller differences—roughly a factor of five—among first-principles models. We investigate the origins

of these differences through comparisons of underlying predictions of ionic and electronic structure. The results of this workshop help to identify plasma conditions where computationally inexpensive approaches are accurate, where computationally expensive models are required, and where experimental measurements will have high impact.

 https://doi.org/10.1063/5.0198155

I. INTRODUCTION

Accurate predictions of the properties of high-energy-density (HED) matter are of critical importance in multiple areas of science, including astrophysics and inertial confinement fusion. The HED regime spans enormous ranges of temperatures and densities, from the warm dense matter of planetary interiors to the hot dense plasma at the hearts of stars. Modeling these systems requires understanding not only the equilibrium properties[1] (equations of state) of matter over this vast range, but also the response (transport) properties[2] of HED matter to gradients in pressure, temperature, and external fields.

Generally, the transport properties of a material are quantified by transport *coefficients* that inform magneto-radiation-hydrodynamic simulation codes and impact the interpretation of data obtained from experimental diagnostics. These data influence our understanding of the development of hydrodynamic instabilities, the overall energy balance of plasma systems, and the efficacy of alpha heating in burning fusion plasmas. Important transport processes include thermal and electrical conduction, energy exchange between ions and electrons, interdiffusion in ionic mixtures, ion viscosity, and charged-particle stopping. Since it is difficult to create and characterize HED matter in the laboratory, simulation codes rely on model predictions for transport coefficients. However, the systematic uncertainties in transport properties obtained from different models or simulation approaches are not well established. Moreover, the statistical uncertainties from a single model or simulation approach are typically not reported.

To quantify the uncertainties—and understand the capabilities—of our current simulation approaches and theoretical models for generating transport coefficients, the first charged-particle transport coefficient comparison workshop[3] was held in 2016. Order-of-magnitude discrepancies were found between different computational approaches, with the largest differences occurring at the lowest temperatures and densities. The second workshop, described here, aimed to (1) add to the data collected in the first workshop, (2) extend the collected quantities for more complete model comparisons to help understand the origin of differences, and (3) select optimal plasma conditions for use in machine learning frameworks[4,5] for uncertainty quantification. The second charged-particle transport coefficient code comparison workshop was held at the University of California's Livermore Collaboration Center (UCLCC) in Livermore, California on 24–27 July 2023. Data were submitted by 39 participants, from 14 institutions, using 18 unique models or simulation approaches.

Section II of this paper provides context for the importance of transport coefficients as closures of the magnetohydrodynamic equations that govern simulations of plasmas. Section III defines and justifies the specific elements, temperatures, and densities selected for this workshop. Section IV gives a brief overview of modeling methods along with a comparison of the submitted results for equilibrium properties including ionic radial distribution functions, electronic densities of states, and average ionization. Section V defines the transport coefficients and presents comparisons of submitted results for ionic transport (shear viscosity and thermal diffusivity), electronic transport (electrical and thermal conductivity), and alpha-particle transport (stopping power). We conclude in Sec. VI with a general discussion and a proposal for cases to be considered in a future workshop.

II. TRANSPORT COEFFICIENTS AS CLOSURES TO THE EQUATIONS OF HYDRODYNAMICS

Transport coefficients quantify how various physical properties relax to equilibrium. These properties include momentum, temperature, and concentration distributions. Conservation laws relate these properties over macroscopic length and time scales. For a single species monatomic gas[6,7] with no external forces the conservation laws are

$$\frac{\partial \rho}{\partial t} + \nabla \cdot (\rho \mathbf{u}) = 0, \tag{1}$$

$$\frac{\partial (\rho \mathbf{u})}{\partial t} + \nabla \cdot (\rho \mathbf{u} \otimes \mathbf{u}) + \nabla \cdot \mathbf{P} = 0, \tag{2}$$

$$\frac{3}{2}\left[\frac{\partial (nT)}{\partial t} + \nabla \cdot (\mathbf{u} nT)\right] + \mathbf{P} : \nabla \mathbf{u} + \nabla \cdot \mathbf{q} = 0, \tag{3}$$

where $\rho \equiv \rho(\mathbf{r}, t) = mn$ is the mass density of the gas defined in terms of the mass m and number density $n \equiv n(\mathbf{r}, t)$, $\mathbf{u} \equiv \mathbf{u}(\mathbf{r}, t)$ is the velocity field of the gas, and $T \equiv T(\mathbf{r}, t)$ is the temperature of the gas, for position vector $\mathbf{r} = x\hat{\mathbf{i}} + y\hat{\mathbf{j}} + z\hat{\mathbf{k}}$ and time t. Additionally, $\mathbf{P}$ denotes the total stress tensor and $\mathbf{q}$ is the heat flow vector. Equations (1) and (2) describe the conservation laws of mass and momentum, respectively, and Eq. (3)—which stems from the conservation of energy—describes the temperature evolution of the gas. In this form, Eqs. (1)–(3) are not "closed"—there are more unknowns than equations. If the gas is in local thermodynamic equilibrium, then a commonly employed choice for the closures is

$$\mathbf{P} = p\mathbf{I} - \eta\left[\nabla \mathbf{u} + (\nabla \mathbf{u})^T - \frac{2}{3}(\nabla \cdot \mathbf{u})\mathbf{I}\right] - \zeta(\nabla \cdot \mathbf{u})\mathbf{I}, \tag{4}$$

$$\mathbf{q} = -\kappa \nabla T, \tag{5}$$

where p is the scalar pressure and $\mathbf{I}$ is the identity matrix. Together, Eqs. (1)–(5) are known as the Navier–Stokes–Fourier equations of hydrodynamics. Now that the stress tensor and heat flow vector have been represented in terms of the gas variables, the last remaining step to close Eqs. (1)–(5) is to quantify the transport coefficients η (the shear viscosity), ζ (the bulk viscosity), and κ (the thermal conductivity). In this workshop, we compare the shear viscosity, η, and the ionic and electronic thermal conductivity—denoted as κ_i and κ_e, respectively. We leave comparisons of the bulk viscosity as a topic for future workshops.

To describe the behavior of current-carrying plasmas, Eqs. (1)–(3) are modified to include additional terms from electromagnetic forces;

they are referred to as the equations of magnetohydrodynamics.[8,9] The equations of magnetohydrodynamics require knowledge of the direct current (DC) electrical conductivity as a closure. In this workshop, we compare values for the *electronic* DC electrical conductivity, σ.

The equations of magnetohydrodynamics underlie large-scale simulations used to describe phenomena in HED systems ranging from the interior of stars and giant planets to terrestrial fusion plasmas. Their closures require understanding the properties of matter at densities and temperatures that are difficult to create in the laboratory and even more difficult to experimentally constrain and measure. In Secs. III–VI, we will describe modeling approaches for computing material properties in HED conditions and compare predictions from multiple models submitted to the second charged-particle transport coefficient comparison workshop.

III. WORKSHOP CASES

The first charged-particle transport coefficient comparison workshop[3] studied H, C, and CH mixtures on a regular grid of temperatures and densities. In this second workshop, we extended the materials to more complex atomic systems and expanded the range of both material conditions and requested data. While the cases in the first workshop provided a wide comparison for two elements (i.e., H and C), a subset of the requested temperature and density range was intractable for many codes and simulation tools. Because of this, the comparison in the first workshop at many conditions was limited to results generated from one or two simulation methods. In this second workshop, we developed a Priority Level System to focus on high-priority cases with the goal of generating more data at targeted points that could be useful for a broader model comparison. The Priority Level System[10] emphasized the importance of the warm dense matter regime, which is relevant to at least the initial stages of most integrated HED experiments; is theoretically challenging due to its combination of thermal effects, electron degeneracy, and strong ion coupling; and is accessible to computationally expensive models. This focus helped to concentrate the efforts of researchers who would only be able to submit data for a handful of cases. Cases in each Priority Level were chosen with consideration of the following criteria:

- Priority Level 1: a minimal set of cases having longitudinal overlap with the first workshop and plasma conditions accessible to multi-atom methods based on density functional theory (DFT);
- Priority Level 2: direct connections to experiments, additional cases having longitudinal overlap with the first workshop, high-value cases determined by data analysis, and conditions accessible to multi-atom DFT-based methods;
- Priority Level 3: data on isochors at densities having longitudinal overlap with the cases of the first workshop and high-value densities determined by data analysis. This Priority Level was accessible to computationally rapid, more approximate models and provided a backdrop for the cases in Priority Levels 1 and 2.

Each case was assigned a Case ID to facilitate the collection and organization of data, structured as "X#" where the leading letter(s) corresponds to the element(s) and the number corresponds to density and temperature values as specified in Table I. While contributors were encouraged to submit results for as many cases and coefficients as possible, it was understood that not all models can generate every quantity and that many models are limited by computational cost.

TABLE I. Requested plasma conditions for the workshop. These cases represent Priority Level 1 and a subset of Priority Level 2. Note that for the mixture cases, the ionic number density $n_{species}$ is given in terms of each species, whereas the mass density ρ_{total} is the total mass density of the mixture. As an example, in case CH1, the number density of each species is $n_H = n_C = 4.63 \times 10^{22}$ cm^{-3}, and $\rho_{total} = (n_H + 12n_C)/N_A = 1$ g cm^{-3}, where N_A is Avogadro's number. Unless otherwise noted, we assume that $T_i = T_e = T$. Recall that in the Case ID column, the number that follows the element does not denote the Priority Level but instead refers to the temperature–density pair for the requested case.

Priority Level	Case ID	Element(s)	$n_{species}$ (cm^{-3})	ρ_{total} (g cm^{-3})	T (eV)
1	H1	H	5.98×10^{23}	1	2
1	C1	C	5.01×10^{23}	10	2
1	CH1	CH	4.63×10^{22}	1	2
1	Al1	Al	6.03×10^{22}	2.7	1
1	Cu1	Cu	8.49×10^{22}	8.96	1
1	HCu1	HCu	1.68×10^{22}	1.8	1
2	Be1	Be	1.23×10^{23}	1.84	4.4
2	CH2	CH	4.16×10^{22}	0.9	7.8
2	Au1	Au	5.91×10^{22}	19.32	10
2	H3	H	5.98×10^{24}	10	20

The Priority Level System was largely successful in focusing the efforts of the contributors, as shown in Fig. 1. Overall, Priority Level 1 cases received more submissions; they also concentrated results from computationally expensive multi-atom DFT-based codes, enabling direct comparisons among different implementations of first-principles models.

	H1	C1	CH1	Al1	Cu1	HCu1	Be1	CH2	Au1	H3
$g(r)$	12/17	11/15	5/7	11/14	6/8	4/4	8/9	4/4	7/8	4/6
DOS(E)	5/17	7/15	4/7	7/14	3/8	1/4	3/9	3/4	5/8	4/6
$Z(t)$	7/17	5/15	2/7	4/14	4/8	1/4	3/9	1/4	3/8	0/6
$C(t)$	5/17	5/15	2/7	4/14	2/8	1/4	1/9	1/4	2/8	0/6
dE_e/dx	5/17	4/15	1/7	3/14	1/8	0/4	2/9	0/4	2/8	2/6
σ	10/17	9/15	6/7	10/14	7/8	3/4	8/9	3/4	6/8	5/6
κ_e	10/17	9/15	6/7	10/14	7/8	3/4	8/9	3/4	6/8	5/6
η	9/17	7/15	2/7	6/14	6/8	3/4	5/9	2/4	5/8	2/6
κ_i	4/17	4/15	0/7	4/14	2/8	0/4	3/9	1/4	3/8	2/6
g	3/17	3/15	0/7	4/14	3/8	0/4	3/9	1/4	3/8	3/6
Z^*	7/17	7/15	2/7	8/14	5/8	0/4	6/9	2/4	6/8	4/6

FIG. 1. Summary of the quantity of received data for the workshop. Each entry displays the number of received data for different observables over the total number of received submissions for each case (see Table I). For example, out of the 17 total submissions for case H1, 12 included data on the radial distribution function, $g(r)$, and 4 included data on the ionic thermal conductivity, κ_i. The entries with the darkest color show the cases with the largest percentage of data received. Overall, fewer data were received for ionic mixtures and the correlation function observables [i.e., $Z(t)$ and $C(t)$]. Computing properties of ionic mixtures—in particular correlation functions—is typically challenging for many of the simulations methods described in Table II.

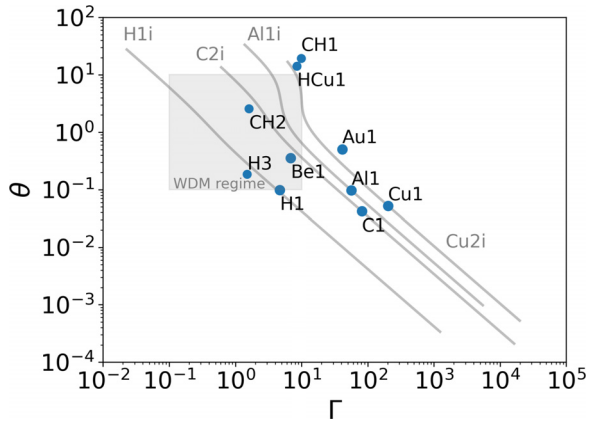

FIG. 2. Electron degeneracy θ and ion coupling Γ parameters of the Priority Level 1 and 2 cases reported here. The curves Al1i, C2i, and Cu2i correspond to Priority Level 3 cases. They denote the isochors corresponding to Priority Level 1 cases Al1, C1, and Cu1, respectively; the curve H1i corresponds to the Priority Level 3 case of H at 1.67 g cm^{-3} (rather than H1's 1.0 g cm^{-3}). The gray square roughly denotes the warm dense matter regime: a challenging regime for many models.

Figure 2 shows where the cases fall in the space of dimensionless plasma parameters Γ, the *Coulomb coupling parameter*, and θ, the *electron degeneracy parameter*. The Coulomb coupling parameter is a common heuristic for estimating the validity of models that assume binary collisions between the ions in a plasma:

$$\Gamma = \frac{(Z^*)^2 e^2}{a_{\mathrm{ws}} T_i}, \tag{6}$$

where Z^* is the average ionization of the ions, e is the electron charge, $a_{\mathrm{ws}} = (4\pi n_i/3)^{-1/3}$ is the Wigner–Seitz radius corresponding to a uniform ion number density n_i, and T_i is the temperature of the ions in energy units. When $\Gamma \gg 1$, the plasma is considered "strongly coupled" and the ions cannot be modeled with binary collisions—one of the fundamental assumptions of the Boltzmann equation for classical plasmas.

The electron degeneracy parameter quantifies the extent to which the electrons will be impacted by Fermi–Dirac statistics. Here, we define the electron degeneracy parameter as

$$\theta = \frac{T_e}{E_F}, \tag{7}$$

where T_e is the electron temperature (in energy units) and $E_F = \hbar^2(3\pi^2 n_e)^{2/3}/2m_e$ is the Fermi energy corresponding to a uniform electron number density n_e. When $\theta \gg 1$, the electron species can be approximated with classical mechanics. While the electrons and ions in a plasma can have different temperatures, in this workshop we have assumed that $T_i = T_e = T$ unless otherwise noted.

The cases in Table I all have fairly large values for the electron degeneracy parameter and moderately to strongly coupled ions. This parameter range is accessible to multi-atom DFT-based codes—the current gold standard for simulating most plasmas with degenerate electrons and strongly-coupled ions. The densities of almost all of the Priority Level 1 cases were included in Priority Level 3 cases for isochoric data, where parameterized and average-atom codes provided a backdrop of data with sufficient temperature resolution to identify important features like conductivity minima and melt transitions. The exception was the H1 case, where the closest corresponding Priority Level 3 case had a density of 1.67 g cm^{-3} (rather than H1's 1.0 g cm^{-3}) to facilitate comparisons to published fractional stopping values.[11]

IV. MODELS AND EQUILIBRIUM PROPERTIES

Transport properties are mediated by interactions among electrons and ions. Approximating these interactions results in model-dependent predictions for atomic-scale equilibrium properties. This includes the screening of partially ionized nuclear cores by bound electrons, the collective behavior of mobile (unbound) electrons, and the distribution of the nuclear cores (atoms or ions). In this section, we describe three categories of modeling approaches, loosely ordered by increasing computational cost: computationally inexpensive parameterized models that use approximations or external input to describe the electronic and ionic properties, quantum average-atom models that compute spherically averaged properties, and multi-atom DFT-based models including Kohn-Sham molecular dynamics and *real-time* time-dependent DFT. All of the codes used in this workshop along with corresponding contributors and model categorizations are listed in Table II; this table serves as a reference with information about approximations made in each of the simulation approaches (e.g., the exchange-correlation functional used) and pertinent references to each approach. This information helps to distinguish models from one another within the data submitted for this workshop. We also present comparisons of submitted data for the average ionization Z^*, the electronic density of states (DOS), and the ionic radial distribution function $g(r)$.

A. Parameterized models

Many hydrodynamic codes rely on fast, inline evaluations of transport coefficients parameterized by the average ionization Z^*. Z^* constrains the effective screening of the nuclear charge from highly localized (bound) electrons and it is critical for highly efficient models of partially ionized plasmas, though it is not uniquely defined. Here, we provide a backdrop for more detailed models using the Lee–More–Desjarlais model (labeled as LMD)[14,50] for electronic transport coefficients as well as a generalized approach to transport described in Refs. 11 and 17 (labeled as SMT) for both electronic[11] and ionic transport coefficients.[17] Two additional models for the ion shear viscosity were included as a backdrop: the Yukawa viscosity model (YVM)[16] and a model based on a Yukawa plasma that leverages the Gibbs-Bogolyubov inequality (YGBI).[15] As part of this workshop the YVM fit has been improved to accurately span hotter temperatures relevant to inertial confinement fusion, and similarly the electronic SMT model has been improved to capture dispersion effects.[32] All aforementioned models use Z^* values from a fit[51] to the Thomas–Fermi (TF) value of Z^* based on a fluid approximation to the response of electrons to a central potential embedded in a plasma—a precursor to modern DFT models. The TF Z^* is given by the gray lines in Fig. 3. Some additional semi-analytic models for plasma transport coefficients can be found in Refs. 52–55.

A second class of parameterized models include those based on kinetic theory (KT) and pair-potential molecular dynamics[57] (MD) models that use input from external sources to inform more sophisticated treatments of screening and transport properties. In this workshop, the KT models included a quantum Landau–Fokker–Planck

TABLE II. Approaches used in this workshop to generate data. The table is organized by model type from lowest computational cost (analytic models) to greatest computational cost (TD-DFT-MD). Note that the organization according to computational cost is only across model types (analytic, KT, AA, DFT-MD, and TD-DFT-MD) and not within each type.

Contributor(s)	Description (code name and version)	Institution(s)	Model type
G. Röpke	Virial expansion[12,13]	U. Rostock	Analytic
L. Stanek	The Lee–More–Desjarlais model,[14] Yukawa–Gibbs–Bogolyubov model,[15] Yukawa viscosity model,[16] and Stanton–Murillo transport model[11,17]	SNL	Analytic
L. Babati, S. Baalrud, N. Shaffer	Mean-force kinetic theory[18–20] using average-atom potentials[21] with temperature-dependent LDA XC functional[22] (Scout)	U. Michigan, LLE	KT
N. Shaffer	quantum Landau–Fokker–Planck kinetic theory with average-atom mean-force electron cross sections[23] (qLFP)	LLE	KT
G. Faussurier	Quantum average-atom model[24–27] (QAAM)	CEA	AA
S. Hansen	Quantum average-atom model with LDA XC functional[28–30] (Bemuze)	SNL	AA
G. Petrov	Average-atom calculation with Dirac exchange[31] (AAM-NRL 4)	NRL	AA
L. Silvestri, Z. Johnson, M. Murillo, G. Petrov	Molecular dynamics simulation with input from TF-Dirac-von Weizsäcker average-atom model and integral equation theory[32] (Sarkas[33])	MSU, NRL	MD
L. Stanek, S. Hansen	Molecular dynamics simulations with interatomic potential from an average-atom calculation (LAMMPS[34])	SNL	MD
M. Bethkenhagen, M. French, R. Redmer, M. Schörner	Quantum molecular dynamics simulation (VASP[35–38] 5.4.4)	LULI, U. Rostock	DFT-MD
A. Blanchet, V. Recoules, F. Soubiran, M. Tacu	Quantum molecular dynamics simulation[39] (Abinit[40–42] 9.7.4)	CEA	DFT-MD
R. Clay, K. Cochrane, A. Dumi, M. Lentz, C. Melton, J. Townsend	Quantum molecular dynamics simulation (VASP[35–38] 6.3.2)	SNL	DFT-MD
S. Hu, V. Karasiev	Quantum molecular dynamics simulation with temperature-dependent TSCANL XC functional in combination with thermal hybrid KDT0 for the Kubo–Greenwood calculation for selected cases (VASP[35–38] 6.2/5.4.4)	LLE	DFT-MD
V. Sharma, L. Collins, A. White	Quantum molecular dynamics simulations with PBE XC functional (SHRED[43])	LANL	DFT-MD
P. Suryanarayana, S. Kumar	Molecular dynamics using on-the-fly machine learning force field with DFT simulation using LDA XC functional (SPARC[44–47])	Georgia Tech.	DFT-MD
A. Kononov, A. Baczewski	TD-DFT simulations with LDA XC functional and bare Coulomb or PAW potentials (VASP[35–38] 5.4.4 extension[48,49])	SNL	TD-DFT-MD
K. Nichols, S. Hu	TD-DFT simulations with PBE XC functional and HGH pseudopotentials (SHRED[43])	LLE	TD-DFT-MD
A. White	Mixed stochastic-deterministic TD-DFT simulations with PBE XC functional and bare Coulomb potentials (SHRED[43])	LANL	TD-DFT-MD

approach to electronic transport properties that uses electron–ion collision cross sections as input[23] and mean-force kinetic theory[18–20] for ionic transport coefficients that uses ion radial distribution functions as input. The MD codes[33,34] for generating data for ionic transport coefficients and correlation functions use interatomic potentials as input. In this workshop, the input quantities are derived either from analytic pair potentials (e.g., Yukawa[17,58,59]), pair potentials obtained from average-atom calculations,[57] or pair potentials from semi-classical methods.[32] These models are slower than models used for inline evaluation, with few-minute runtimes for KT and tens-of-minutes runtimes for MD, but they are expected to provide higher fidelity data than fully parameterized models. While these parameterized models can offer a large reduction in computational cost compared to the models discussed in Sec. IV C, their efficacy is heavily dependent on the quality of their inputs and the flexibility of their parametric form.[57]

B. Average-atom models

Average-atom models[21,27,28,60,61] describe the electronic structure surrounding a single, averaged ion suspended in jellium. All of the average-atom models contributed to this workshop use Kohn–Sham orbitals to compute the electronic structure; we will use the term "quantum-AA," or simply AA, to denote average-atom models of this type. Following the pioneering work of Liberman,[62] these all-electron, fully quantum models find a converged electron–ion potential (including approximate exchange and correlation effects) that supports a

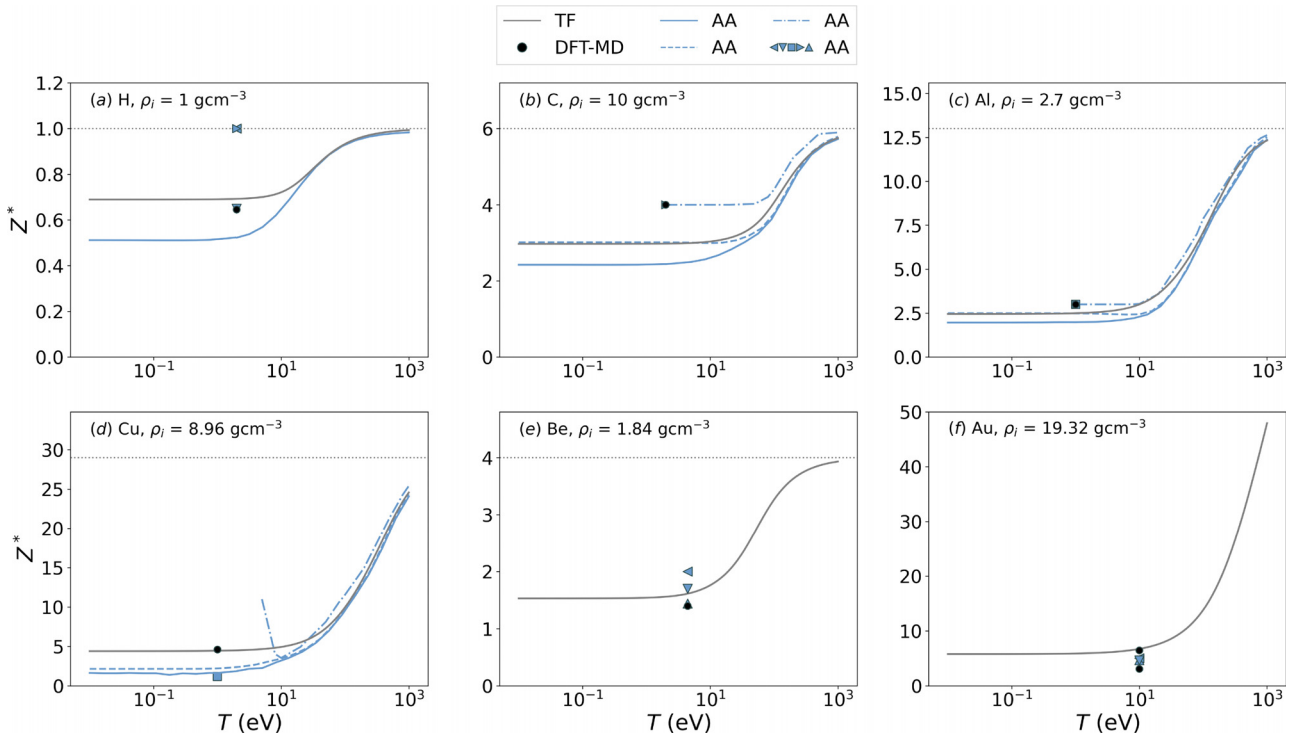

FIG. 3. Average ionization Z^* for some of the single-species cases detailed in Table I. Horizontal lines indicate the bare ion charge for reference. Because Z^* can be defined in multiple ways,[56] there is significant variation across models and even within the same type of model: the quantum-AA models shown here use different definitions for Z^*.

self-consistent set of electronic orbitals. These orbitals provide information on the radial electron density and the energy-dependent electronic density of states (DOS). The densities of states from two independent AA models are shown in Fig. 4.

Several definitions of Z^*[56] can be extracted from AA models and used to parameterize the methods described in Sec. IV A. In Fig. 3, for example, some of the AA models define Z^* to include all occupied positive-energy orbitals while others count only the plane wave (ideal) portion of occupied orbitals as free electrons. The first definition can result in discontinuities in Z^* as orbitals move from negative (bound) to positive energies, while the second definition gives smoother behavior more similar to the TF fit. It is notable that while several independent quantum-AA models give widely different predictions for Z^*, their underlying electronic densities of state are virtually identical. The choice of Z^* also influences AA-model predictions for ion–ion interaction potentials, which can be used to determine (spherically symmetric) ionic radial distribution functions[63] and ion–ion transport coefficients.[57]

While AA models are relatively efficient, with runtimes of several minutes, and they are expected to be more accurate than Z^*-parameterized models for plasmas and liquids, they cannot account for bonding or crystalline effects that are important at low temperatures. They also do not calculate transport properties directly without appealing to additional models. For example, from their self-consistent set of electronic and ionic properties, AA models can derive electron–ion collision rates through the Ziman equation[27,64,65] that inform electronic transport properties. Coupled with a model for stopping numbers or dielectric functions, AA models can also calculate stopping powers.[27,30]

C. Multi-atom DFT models

The final category of models in this workshop are based on a DFT description of a multi-atom system, including Kohn–Sham molecular dynamics[49,66–74] (DFT-MD, also known as quantum molecular dynamics or QMD) and *real-time* time-dependent DFT[75] (TD-DFT). These first-principles models self-consistently solve for a three-dimensional electron density interacting with an ensemble of ions. DFT-MD then simulates ps-scale ion dynamics with interatomic forces determined by the equilibrium electronic structure at each time step. This separation of electronic and ionic time scales is known as the Born–Oppenheimer approximation. In contrast, TD-DFT models fs-scale dynamics of electronic excitations in response to an external perturbation. To capture ionic disorder, TD-DFT simulations in this workshop began from equilibrated structures obtained from DFT-MD and thus we denote this model as TD-DFT-MD.

Within DFT-MD, ionic transport properties are extracted from integrals of autocorrelation functions. Electronic transport properties are extracted from the Kubo–Greenwood[76,77] formalism, with dynamic properties averaged over ionic configurations and extrapolated to zero-frequency for DC limits. A Kubo relation has also been proposed for electron–ion temperature relaxation rates from DFT-MD,[78,79] but was not applied in this workshop. While TD-DFT-MD can offer an alternative framework for accessing electronic transport properties,[80,81] contributions to this workshop only use this method to

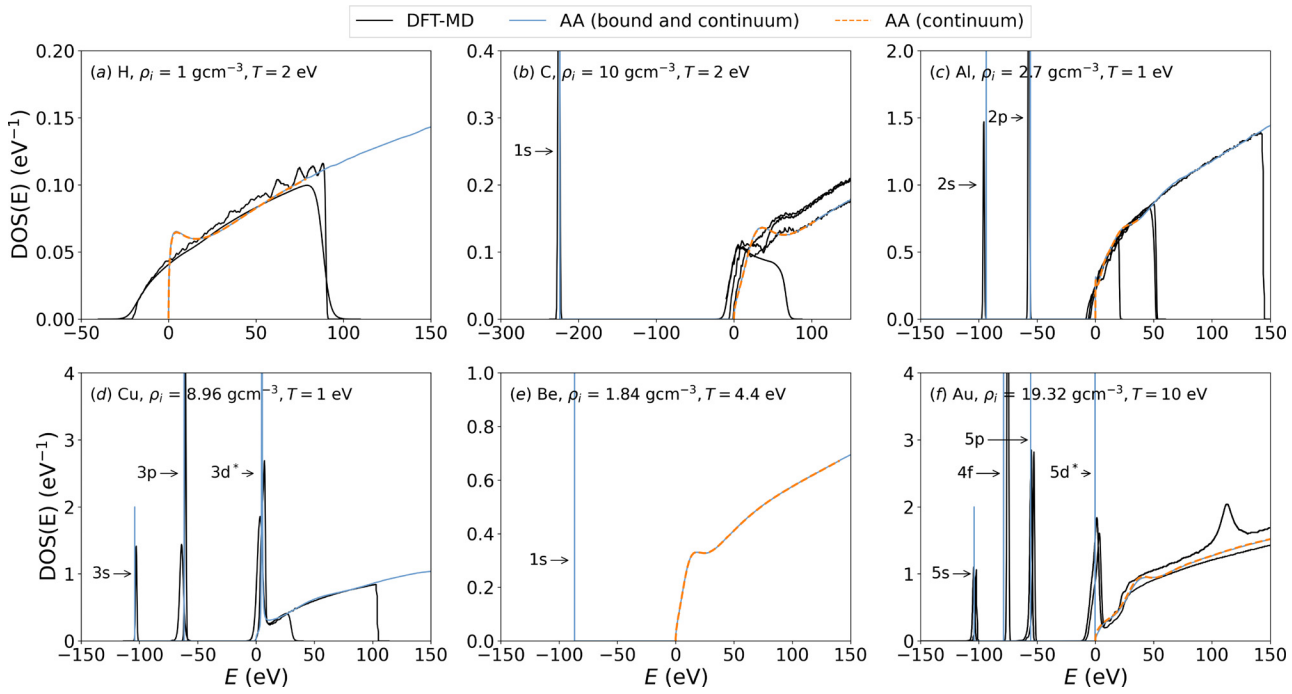

FIG. 4. Electronic densities of states for some of the single-species cases in Table I. Bound states are labeled for each applicable element. All models have been shifted (to the best of our ability) to the same energy scales, as determined by the binding energies of negative-energy states and the reported chemical potentials (or Fermi energies). Two independent AA models (one model reported both bound and continuum electrons and another reported only the continuum electrons) have virtually identical DsOS, which reproduce the general features of the multi-atom DFT DsOS quite well except for the carbon case. The positive-energy feature in the DFT-MD model of Au near $E = 120$ eV is believed to be an artifact of the pseudopotential. Multi-atom models tend to predict broader features than AA models due to both variations in the local fields of different atomic centers and, in some implementations, imposed broadening. The positive-energy DsOS from multi-center models artificially drop to zero at different energies, depending on how many continuum states the particular calculation included.

predict electronic stopping powers by simulating electron dynamics as an alpha particle traverses the plasma. The stopping power is determined by the average force exerted on the alpha particle by the electronic system, or equivalently, the average rate at which the alpha particle deposits energy into electronic excitations.[82]

Both DFT-MD and TD-DFT-MD are fundamentally characterized by an approximate choice of exchange and correlation (XC) potential to describe the mean-field electron–electron interaction, an approximation that also enters AA models.[12] Additionally, these methods typically employ pseudopotentials to avoid large computational costs associated with highly oscillatory wavefunctions near ion cores. Nonetheless, the multi-atom and three-dimensional nature of DFT-MD and TD-DFT-MD allows these methods to describe interatomic bonding and anisotropic behavior. They also treat bound and free electrons on the same footing without relying on a state partitioning or Z^* definition. In practice, rigorous application of these DFT-based models requires preliminary calculations to ensure convergence with respect to numerical parameters and quantify sensitivity to model choices like XC potentials and pseudopotentials.

Systematic improvements of XC functionals have been performed along the so-called Jacob's ladder.[83] Its lowest rung is the local density approximation (LDA) followed by the generalized gradient approximation (GGA). Each higher rung of the ladder such as meta-GGAs and hybrid functionals represents an improved approximation for the total energy calculated within DFT.

These DFT-MD and TD-DFT-MD models represent the state of the art for HED materials properties calculations. While these models still have difficult-to-quantify systematic errors, they are computationally viable over a wide range of conditions from ambient materials to warm dense matter, and strong empirical evidence indicates that their accuracy suffices for many relevant applications. Their predictions for ionic radial distribution functions generally agree well with directly observable x-ray diffraction measurements; we illustrate radial distribution functions, $g(r)$, in Fig. 5 for some of the cases of Table I. However, multi-atom DFT calculations are computationally expensive, consuming many hours—or weeks—of CPU time, and they can become intractable or require further approximation for high temperatures and many-electron ions. To reduce computational expense, the number of ions may be restricted (potentially leading to finite-size effects[57]), the electrons within ion cores may be included in psuedopotentials (approximating their behavior), and/or sub-cubic scaling algorithms that rely on sparsity or stochastic sampling may be applied.[43,45,84–86]

V. TRANSPORT COEFFICIENTS

In this section, we describe how transport coefficients are computed within the atomic-scale modeling approaches described above and show comparisons of the results submitted to this workshop. For clarity and discussion of the results, we divide this section into four parts: electronic transport coefficients (electrical and thermal

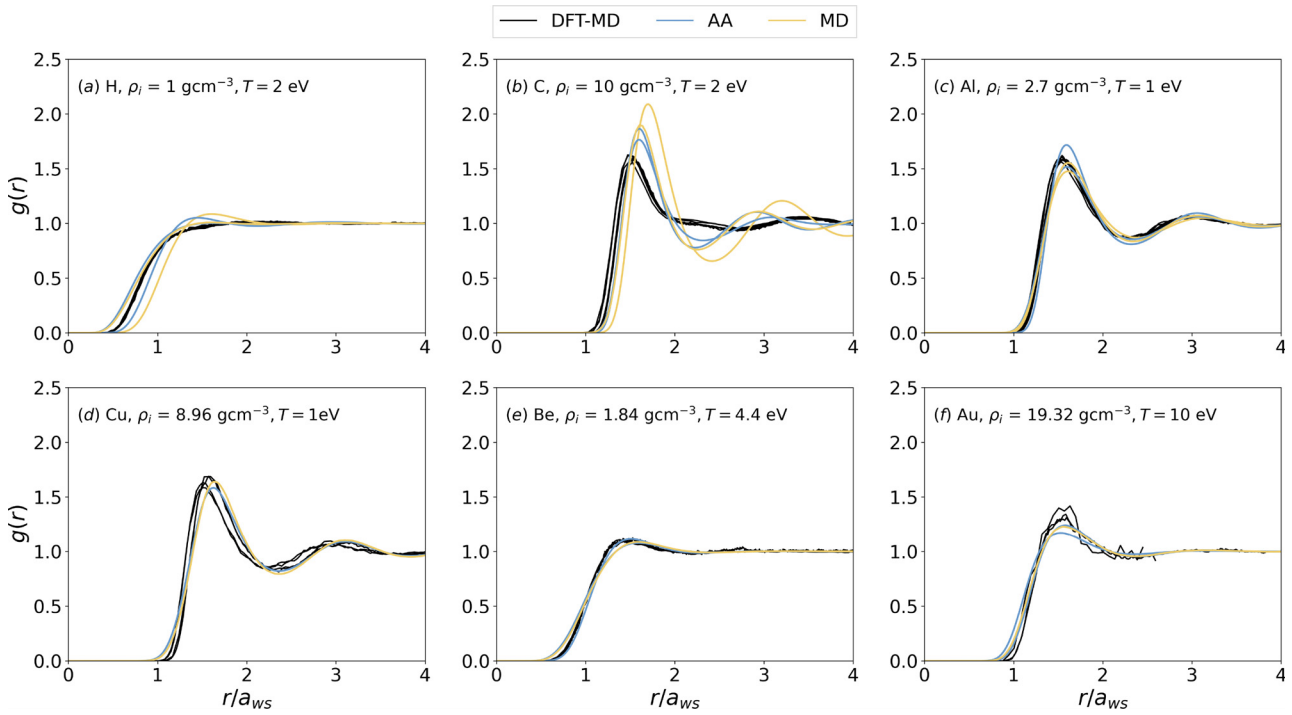

FIG. 5. Ionic radial distribution function, $g(r)$, for some of the single-species cases in Table I. $g(r)$s from AA models are obtained by solving the quantum Ornstein–Zernike equations and employing the hyper-netted chain approximation while $g(r)$s obtained from DFT-MD and MD models are obtained directly from ensemble-averaged particle positions.

conductivities; Sec. V A), ionic transport coefficients (shear viscosity and thermal diffusivity; Sec. V B), electron–ion temperature relaxation rate (Sec. V C), and stopping power (Sec. V D).

A. Electronic transport coefficients

In the warm dense regime, electronic transport coefficients—such as DC electrical conductivity and the electronic thermal conductivity—are governed by collisions between mobile electrons and collisions between mobile electrons and static ions. In classical and fully ionized plasmas, collisions are often treated using Coulomb logarithms based on minimum and maximum approach distances. For the partially ionized and partially degenerate plasma cases considered in this workshop, the calculations require a more complete treatment of collisions.

In general, the DC electrical conductivity can be computed via

$$\sigma = L_{11}, \tag{8}$$

where L_{ij} denote the Onsager coefficients,[87–89] which are related to detailed balance among collisional rates. The electronic thermal conductivity is also represented by Onsager coefficients and has the form

$$\kappa_e = \frac{1}{T}\left(L_{22} - \frac{L_{12}^2}{L_{11}}\right). \tag{9}$$

In practice, the codes contributing to this workshop treat electronic transport properties in quite distinct ways. Most of the codes designated as KT in Table II use an effective Boltzmann approach that requires an effective interaction potential; the potentials may be specified generically[11,17] or computed on a case-by-case basis.[18,90,91] Once an effective potential is obtained, the KT codes numerically evaluate collision integrals—avoiding the need for a Coulomb logarithm. The KT codes then utilize the Chapman–Enskog approach[92,93] to determine the relevant transport coefficients. A primary source of uncertainty in KT codes of this kind results from the choice of the effective interaction potential.

Most of the codes designated as AA use modifications of the Ziman approach[27,64,65] to calculate electron–ion collision rates, integrating over both ionic and electronic structure. The DFT-MD codes obtain the DC conductivity by extrapolating the frequency-dependent conductivity obtained by Kubo[76] and Greenwood[77] relations to the zero frequency limit.[94,95] This extrapolation is often a significant source of uncertainty for evaluating the DC conductivity from multi-atom DFT-MD-based models. A description of the extrapolation procedure and other considerations for computing the Onsager coefficients, and thus the electronic and thermal conductivity, from multi-atom DFT-MD codes can be found in Refs. 96 and 97. Another source of uncertainty for the evaluation of the electronic transport coefficients is the mean-field treatment of electron–electron interactions.[12,96] The method of DFT-MD plus Kubo–Greenwood has been used to calculate thermal conductivities of materials relevant for inertial confinement fusion (e.g., D and CH) in a wide range of densities and temperatures.[95,98–100] The results are generally larger than what traditional plasma models predict in the WDM regime, which was aligned with AA prediction and recent experiment.[101] A thorough review on this is given by Ref. 102 in this special issue.

Comparisons of the submitted data for the DC electrical conductivity σ and electronic thermal conductivity κ_e are given in Figs. 6 and 7, respectively; the corresponding data are provided in Tables V and VI.

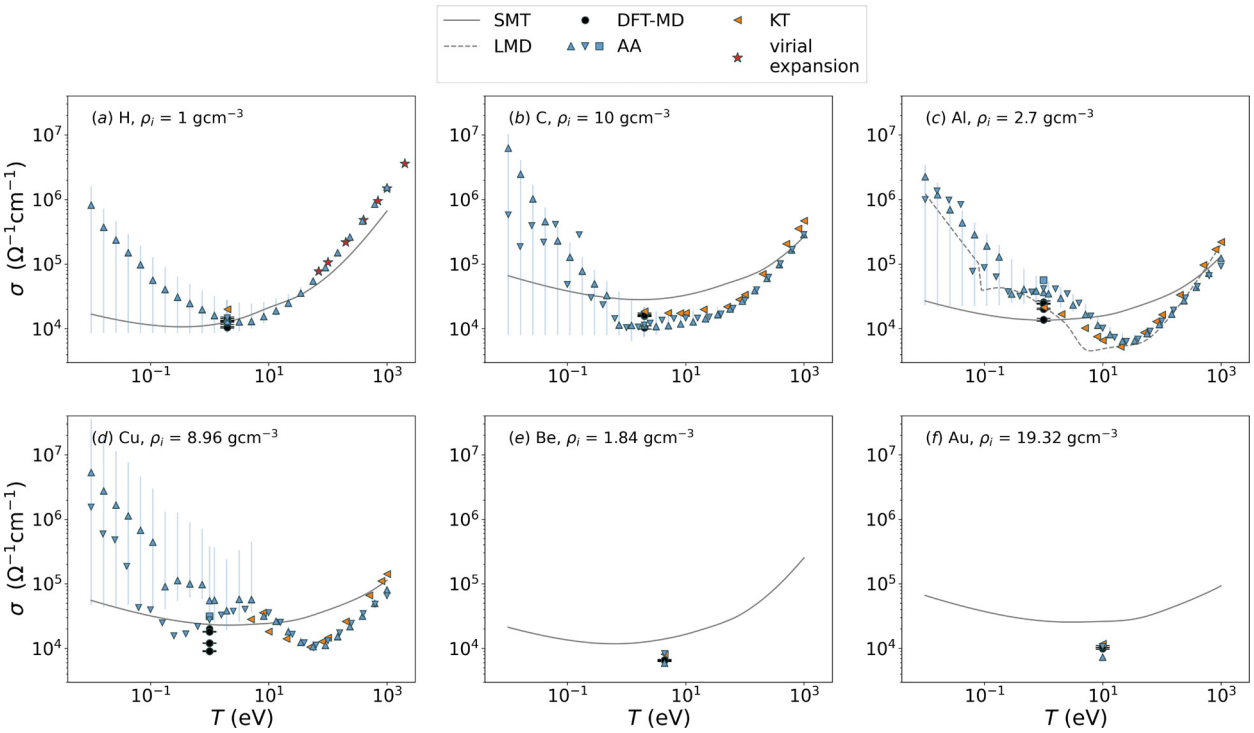

FIG. 6. Electrical conductivities for some of the single-species cases in Table I. For one of the AA models (upward pointing triangles), error bars are given indicating the possible range for different choices of ion structure and average ionization Z^*. Another AA model (downward pointing triangles) shows discontinuities from unconverged cases. The DFT-MD results are concentrated at the cases defined in Table I.

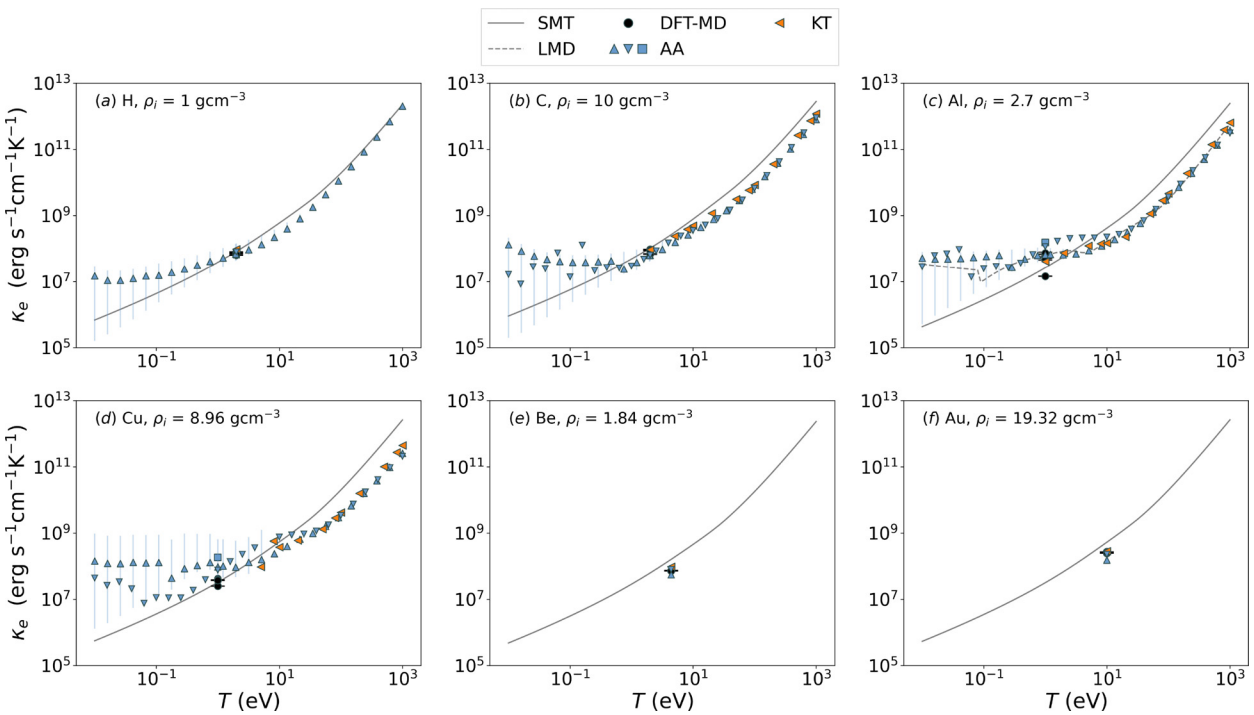

FIG. 7. Same as Fig. 6, but for electron thermal conductivities.

Of the submitted data in Priority Level 1 and 2 cases, the greatest difference appears in the cases of Al1 and Cu1. The maximum difference between all models for the DC electrical conductivity is roughly a *factor of seven* for case Cu1. This difference decreases if we consider the differences within a single model type. For a single model type, the maximum difference in the DC electrical conductivity is roughly a *factor of two*—which occurs between the AA models of case Cu1. For the electron thermal conductivity, the maximum difference between all models—which occurs for case Al1—is roughly *one order of magnitude*; the maximum difference within a single model type is roughly a *factor of five* which occurs between DFT-MD models for case Al1. These differences are much larger than those observed in the electronic densities of states or even Z^* values (among models reliant on a Z^* definition), which should together largely determine the electron–ion interaction.

The modest disagreement among DFT-MD models may be attributable to several factors arising from the finite size of the simulations, which produces a discrete spectrum of allowable low-energy electronic transitions. A *broadening* procedure—as discussed in Ref. 96—recovers continuous optical conductivities, but these are only accurate above the minimum captured transition energy. Thus, the DC limit requires extrapolation using fit functions of known forms (e.g., the Drude model), which may not be accurate for all materials. Also, the extrapolated values converge slowly with the number of particles in the simulation, and multiple DFT-MD simulations are typically carried out at increasing particle number. In this workshop, the typical number of particles that participants employed in their DFT-MD calculations ranged from *tens to hundreds*. Despite all these choices, the DFT-MD models tend to agree better with one another than with AA or parameterized models.

The larger disagreement among AA models, which perform an all-electron calculation for a single atom, is also attributable to a combination of factors. These models are heavily dependent on choices for Z^* and the ionic structure factor. Variations due to different possible choices of these quantities are illustrated by the error bars on the points from one submitted AA model in Figs. 6 and 7. Most (but not all) of the independent AA models fall within the range defined by these variations. While the fully parameterized SMT and LMD models have yet larger differences, both among themselves and with the quantum-AA and DFT-MD models and especially at low temperatures, the AA-informed kinetic theory models are in encouraging agreement with AA models at high temperatures.

There is very little experimental data to provide guidance on electrical and thermal conductivities in warm and hot dense matter due to the difficulty of creating sufficiently uniform states of matter in these extreme conditions, independently characterizing their temperature and density, and measuring or inferring the conductivities. Many experimental approaches to measuring these transport coefficients have a significant co-dependence on the equation of state[101,103–107] and/or probe the optical response far from the DC limit.[108,109] Recent advances with THz probes coupled with x-ray diffraction measurements at x-ray free-electron laser facilities[110] offer a promising approach to experimental validation.

B. Ionic transport coefficients

Ionic transport coefficients are governed by collisions among ions. In partially ionized systems, these collisions are mediated by electron distributions that screen long-range forces between ions. If binary collisions are assumed between ions, KT codes that use an effective Boltzmann approach[17,18] (see Sec. V A) can be employed to estimate the ionic transport coefficients. Because these methods are based on a Boltzmann kinetic theory framework, KT codes are most accurate for weakly coupled plasmas. In contrast, one could simulate a system of interacting particles using MD to go beyond the binary collision approximation. Approaches for estimating ionic transport coefficients using particle trajectories from MD are discussed in the paragraphs that follow.

The shear viscosity—also referred to as the *dynamic* viscosity—quantifies the magnitude of a fluid's response due to gradients in fluid velocity. The shear viscosity η may be computed by the Green–Kubo relation

$$\eta = \frac{1}{Vk_BT}\int_0^\infty dt\,\langle P_{\gamma\beta}(t)\,P_{\gamma\beta}(0)\rangle, \tag{10}$$

where V is the volume of the system, k_B is the Boltzmann's constant, T is the system temperature, $\gamma, \beta \in \{x, y, z\}$ are Cartesian indices, and $P_{\gamma\beta}$ denotes an off diagonal component of the pressure tensor,[111] i.e., $\gamma \neq \beta$. The brackets $\langle\cdot\rangle$ denote an ensemble average over thermodynamic configurations. The averaging may be done over multiple independent MD simulations or by partitioning a single MD simulation into uncorrelated samples. The ion thermal conductivity may also be defined in terms of a Green–Kubo relation, namely,

$$\kappa_i = \frac{1}{Vk_BT^2}\int_0^\infty dt\,\langle j^e_\gamma(t)\,j^e_\gamma(0)\rangle, \tag{11}$$

where j^e_γ denotes the γ-component of the energy current.[111] By exploiting isotropy of the systems considered here, we can average the results of the integrals appearing in Eqs. (10) and (11) for all γ, β, yielding a more statistically accurate result.

From Eq. (11), the ion thermal diffusivity is defined by

$$\alpha \equiv \frac{\kappa_i}{\rho_i c_p}, \tag{12}$$

where c_p denotes the specific heat capacity at constant pressure. For monatomic gasses, an approximation for the specific heat capacity is $c_p \approx 20.785\,\mathrm{J\,K^{-1}\,g^{-1}}/A$, where A denotes the relative atomic mass. In practice, values for c_p are obtained from a numerical derivative of the enthalpy generated from "lookup" tables of energy and pressure values. In Table III, we compare the monatomic approximation to that generated from a "lookup" table approach with pressures and energies derived from effective ionic potentials. We see that for case C1, the monatomic gas approximation and MD results differ by nearly a factor of four.

Here, we compare the shear viscosity, η, and the ion thermal conductivity, κ_i. The data received for the shear viscosity are presented in Fig. 8 and data for the thermal conductivity—which is cast in terms of the thermal diffusivity using Eq. (12)—are displayed in Fig. 9; the data of these coefficients are given in Tables V and VI. Of the data received for the shear viscosity, we find that the maximum difference between all data submitted for a given Priority Level 1 or 2 case is roughly a *factor of twenty*; the maximum difference occurs for the case C1. While this difference is substantial, it is not unexpected if we consider the disparate approaches and models used for computing the shear viscosity. In particular, results for obtaining the shear viscosity from Eq. (10) are

TABLE III. Mass density times ionic specific heat at constant pressure, $\rho_i c_p$. The column denoted $\rho_i c_p^{\text{eff}}$ indicates that c_p has been computed from an effective ionic potential approach—submitted by L. Silvestri (see Table II for the full list of contributors); the column denoted $\rho_i c_p^{\text{mon}}$ indicates that c_p has been computed from the relation for the monatomic gas as mentioned in the main text.

Case ID	$\rho_i c_p^{\text{eff}}\left(\frac{\text{erg}}{\text{Kcm}^3}\right)$	$\rho_i c_p^{\text{mon}}\left(\frac{\text{erg}}{\text{Kcm}^3}\right)$	$\frac{\rho_i c_p^{\text{eff}}}{\rho_i c_p^{\text{mon}}}$
H1	1.91×10^{8}	2.06×10^{8}	0.93
C1	6.35×10^{8}	1.73×10^{8}	3.67
Al1	4.14×10^{7}	2.08×10^{7}	1.99
Cu1	...	2.93×10^{7}	...
Be1	...	4.24×10^{7}	...
Au1	...	2.04×10^{7}	...
H3	...	2.06×10^{9}	...

expected to be more accurate in the strong-coupling regime in contrast to expressions that rely on numerically evaluated collision integrals or from approaches that only require the collision rate as input. If instead we consider the difference between similar models within a given case, we find that the maximum difference is roughly a *factor of six* for case HCu1 which occurs between DFT-MD models.

Similarly, we find that of the data received for the ion thermal conductivity, the maximum difference between all models is on the order of *one order of magnitude* (for cases C1 and Al1), and that the maximum difference within a given model type is roughly a *factor of seven* for case C1 between MD models. These results are consistent with the differences in the self-diffusion coefficient calculated from a variety of pair-interaction potentials used in MD simulations of dense plasmas[57] where the maximum differences were on the order of ten between pair-potential models.

The discussion of results up to this point has been on the uncertainty *between* models. We now switch our discussion to the statistical uncertainty incurred when using a single model. Depending on the model used to generate the transport coefficient data, there are multiple ways statistical uncertainties manifest. In particular, for MD simulations, statistical uncertainties occur from the inability to simulate an infinite number of particles (often referred to as uncertainty from *finite-size effects*[57]) the truncation of the upper bound on the integrals defined in Eqs. (10), (11), and (14), and uncertainties due to the incomplete sampling of the thermodynamic ensemble during the MD simulation. By carrying out multiple MD simulations—at the same plasma conditions—but with an increasing number of particles, one can estimate uncertainties due to finite-size effects (see Ref. 57). Statistical noise in the integration of the expressions in Eqs. (10), (11), and (14) can be mitigated by utilizing appropriate fit functions[112] and by exploiting stationarity of the autocorrelation function.[111]

Equations (10) and (11) are integrals over autocorrelation functions, e.g., the stress autocorrelation function for the shear viscosity. Because transport coefficients are integrated quantities, it is useful to compare the autocorrelation functions generated by the various simulation approaches. In this workshop, we requested data for two autocorrelation functions: the velocity autocorrelation function and the stress autocorrelation function. The normalized velocity autocorrelation function is defined as

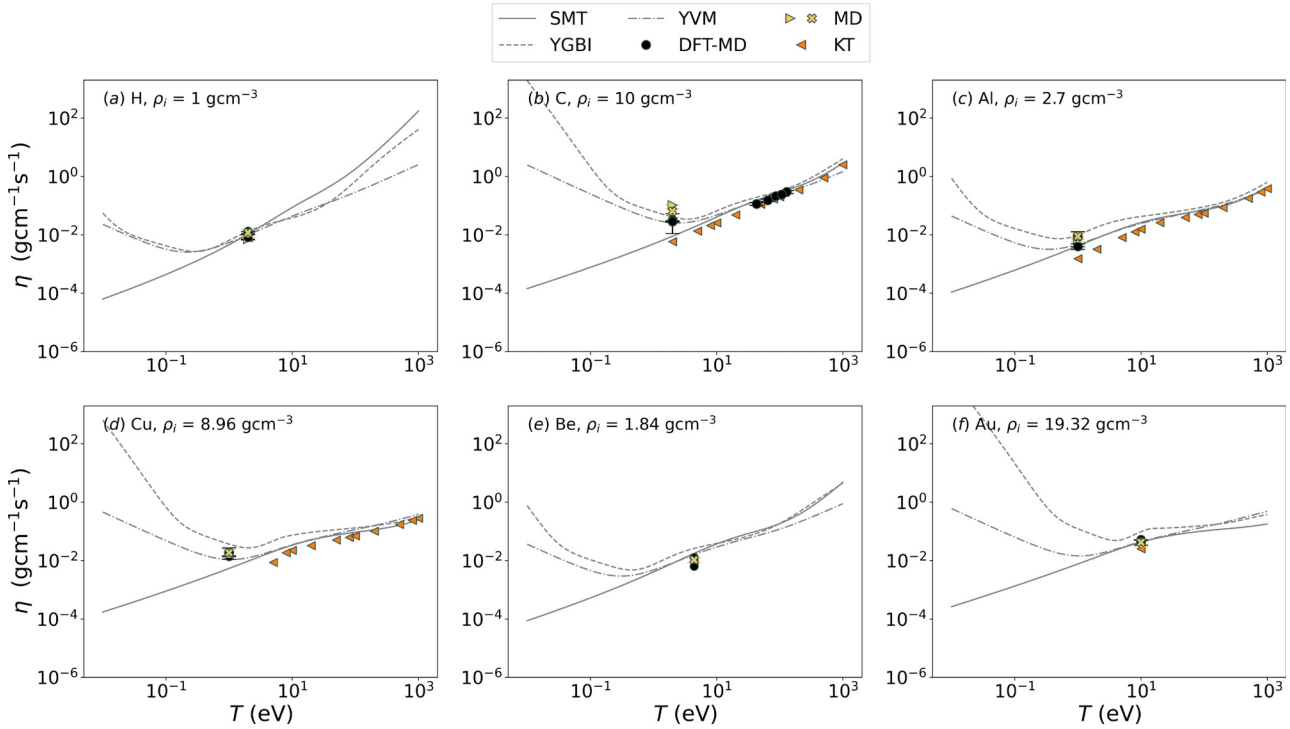

FIG. 8. Ion shear viscosity η for some of the single-species cases in Table I.

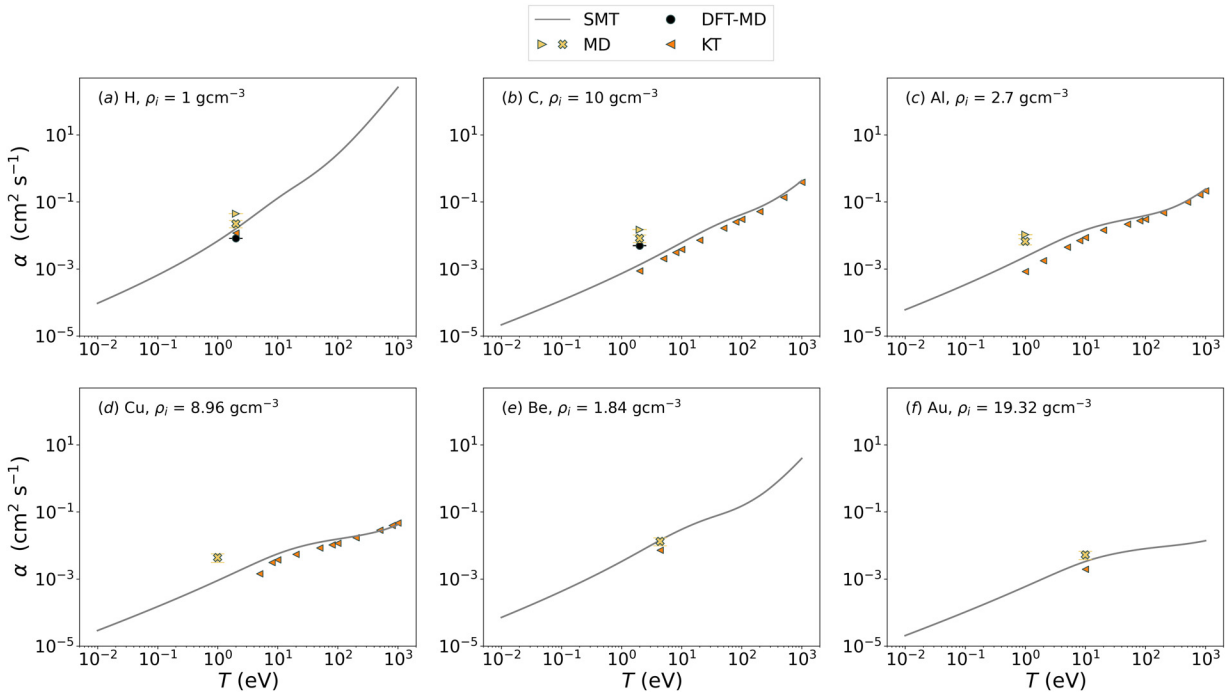

FIG. 9. Thermal diffusivity α for some of the single-species cases in Table I.

$$Z(t) \equiv \frac{\langle \mathbf{v}(t) \cdot \mathbf{v}(0) \rangle}{\langle \mathbf{v}(0) \cdot \mathbf{v}(0) \rangle}, \tag{13}$$

where $\mathbf{v}(t)$ denotes the velocity vector of a particle at time t. Equation (13) is the integrand of the Green–Kubo relation for the self-diffusion coefficient D, where

$$D = \frac{T}{m} \int_0^\infty dt\, Z(t). \tag{14}$$

We note that the self-diffusion coefficient does not appear in the single-species hydrodynamics equations (1)–(5), nor does it appear in the multi-species case. However, the velocity autocorrelation function is a useful metric for comparing dynamical properties of the system by providing insight into differences in integrated observables (e.g., transport coefficients). Similarly, the normalized stress autocorrelation function is given by

$$C(t) \equiv \frac{\langle \bar{P}(t) \bar{P}(0) \rangle}{\langle \bar{P}(0) \bar{P}(0) \rangle}, \tag{15}$$

where $\bar{P}(t) \equiv [P_{xy}(t) + P_{yz}(t) + P_{xz}(t)]/3$.

As concrete examples of how the autocorrelation functions were computed in this workshop, we turn to the data received from the two models denoted MD (see Table II). For these data, on the order of *thousands* of particles were used in each simulation. Then, on the order of *tens* of MD simulations were carried out with differing initial conditions (particle placement and velocity) for each case. The autocorrelation functions from each simulation were averaged to obtain an average autocorrelation function which is used to estimate the pertinent transport coefficients. A block averaging scheme may also be employed[111] in each MD run to reduce statistical noise.

In Fig. 10, we show a comparison of the normalized velocity autocorrelation function [Eq. (13)] for the models described in Table II. The only methods in Table II that can directly compute the velocity autocorrelation function are DFT-MD and MD as they are the only approaches that directly simulate the motion of particles over sufficiently long time scales. In Fig. 10, we observe that in most cases, the DFT-MD simulation methods generally agree—most notably in terms of the autocorrelation time. In contrast, the MD simulation methods appear to agree in some cases, but disagree in other cases; the differences in the representation of $Z(t)$ are directly related to the choice of interatomic potential used in the MD simulations. We caution that even though $Z(t)$ can vary between models, the self-diffusion coefficient obtained by integrating $Z(t)$ using Eq. (14) can be approximately the same.[57] A similar comparison is displayed in Fig. 11 where we show the stress autocorrelation function [Eq. (15)].

From Figs. 10 and 11, three things are clear. First, due to the significant computational cost, the DFT-MD based simulation approaches are often plagued by finite-size effects—appearing as noise in the autocorrelation functions. Second, in contrast to $Z(t)$, $C(t)$ requires a longer simulation time to converge to a meaningful result. Third, the autocorrelation time varies between models.

C. Electron–ion temperature relaxation rate

While conductivity is governed by momentum scattering frequencies, temperature relaxation in non-equilibrium plasmas is governed by the energy exchange between ions and electrons. For example, in the two-temperature model, the energy exchange is described by the coupled equations

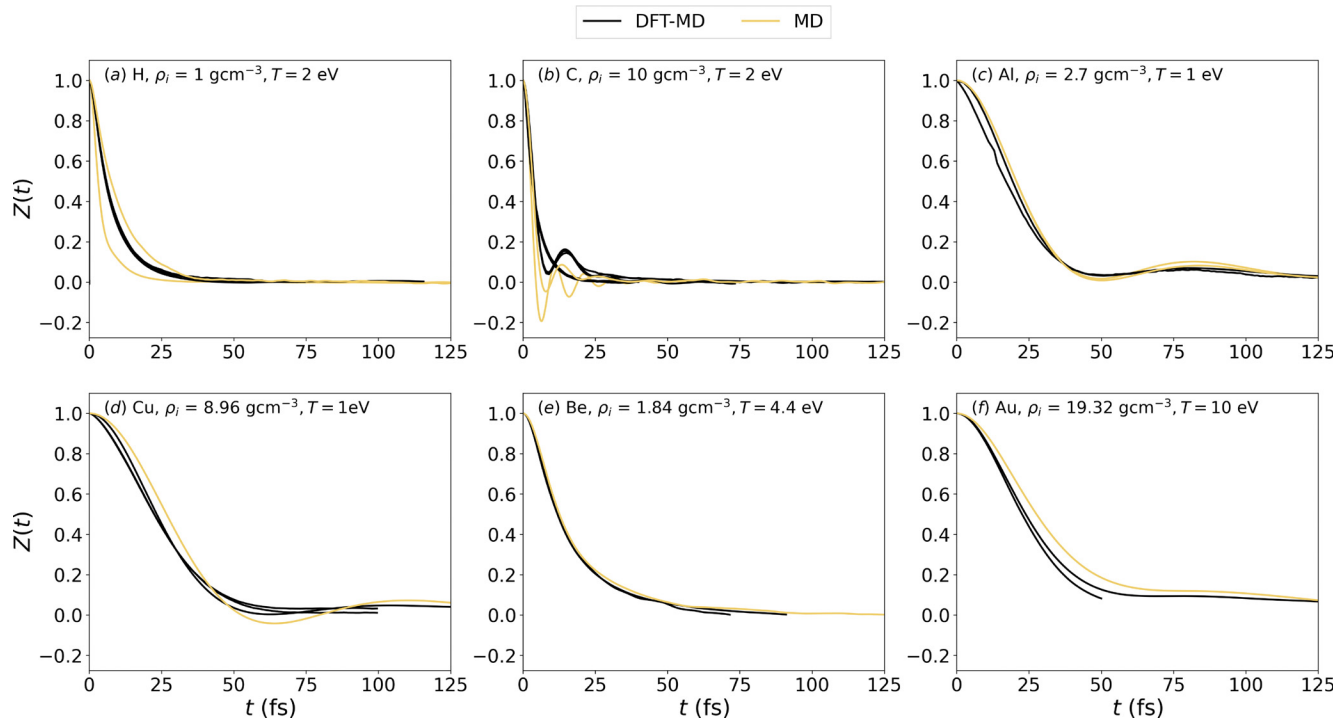

FIG. 10. Normalized velocity autocorrelation function $Z(t)$ [Eq. (13)] vs time for some of the single-species cases in Table I.

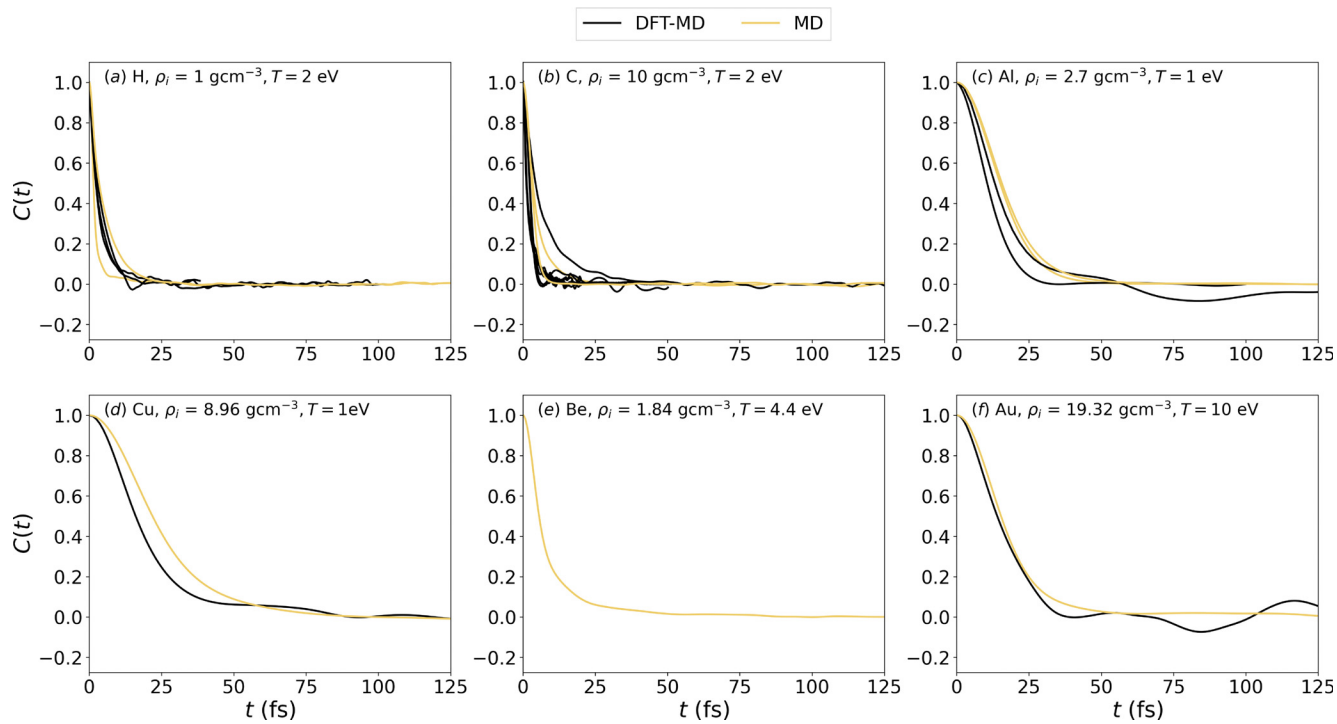

FIG. 11. Normalized stress autocorrelation function $C(t)$ [Eq. (15)] vs time for some of the single-species cases in Table I.

$$C_e \frac{dT_e(t)}{dt} = -g[T_e(t) - T_i(t)], \quad (16)$$

$$C_i \frac{dT_i(t)}{dt} = g[T_e(t) - T_i(t)], \quad (17)$$

where C_e and C_i are the heat capacity of the electrons and ions, respectively, and g is the electron–ion temperature relaxation rate. Note that Eqs. (16) and (17) are a simplified form of the general two-temperature model.[113] Here, we have assumed there is no external source term, there is no heat flux, and that the heat capacity terms are independent of temperature. Finally, we note that calculations of dT/dt that include heat capacities native to a given model could enable more direct comparisons with experimental data than calculations of g, since experiments measure temperature as a function of time.[114,115] Most contributors of this workshop generate g from collision rates which would represent equilibration rates at a small perturbation from $T_e = T_i$—much like collisions for conductivity are determined in the presence of a weak electric field. In practice, these calculations are relatively insensitive to T_i. Submitted values of g are given in Tables V and VI.

D. Stopping power

Finally, we compare electronic stopping powers for alpha particles traversing some single-species plasma cases as specified in Table I. Data for the electronic stopping powers are displayed in Fig. 12, and provided in Table VII, which additionally includes data for the CH1 and H3 cases. The two AA models differ mainly in the low-velocity regime, likely due to different parameterizations of the stopping number in a uniform electron gas. TD-DFT-MD is generally expected to be more accurate and can serve as a valuable benchmark for AA models.[30] However, the high computational cost of TD-DFT-MD calculations limited this method to a subset of the Priority Level 1 cases illustrated in Figs. 12(a)–12(c).

Figure 12(a) includes several TD-DFT-MD datasets for alpha-particle stopping in case H1 that were computed using different codes and methodological details, including deterministic vs mixed stochastic-deterministic TD-DFT variants, HGH pseudopotentials vs bare Coulomb potentials, and LDA vs PBE XC functionals. Additionally, some of the TD-DFT calculations optimized the alpha-particle trajectory to representatively sample a cubic simulation cell and mitigate finite-size effects,[73] whereas others used an elongated simulation cell with the alpha particle traveling along the long direction.

Nonetheless, the different TD-DFT-MD stopping power datasets in Fig. 12(a) agree amongst each other quite well, and the minor discrepancies reflect the sensitivity that even this first-principles model can have to methodological choices. Furthermore, high computational costs can make it challenging to assess convergence and quantify uncertainties in TD-DFT-MD stopping powers. A separate article within this special issue scrutinizes the sources of these small discrepancies and finds highest sensitivities to the pseudopotential approximation, finite-size errors, and alpha-particle trajectory choice.[116]

In Fig. 12(a), all of the TD-DFT-MD datasets agree quite well with both average-atom models beyond the stopping power peak. Good agreement is also obtained for case C1 shown in Fig. 12(b), where one TD-DFT-MD dataset included contributions from C 1s electrons and the other excluded them through the use of pseudopotentials. For case Al1 of Fig. 12(c), however, both AA models significantly exceed the TD-DFT-MD predictions. To reduce computational

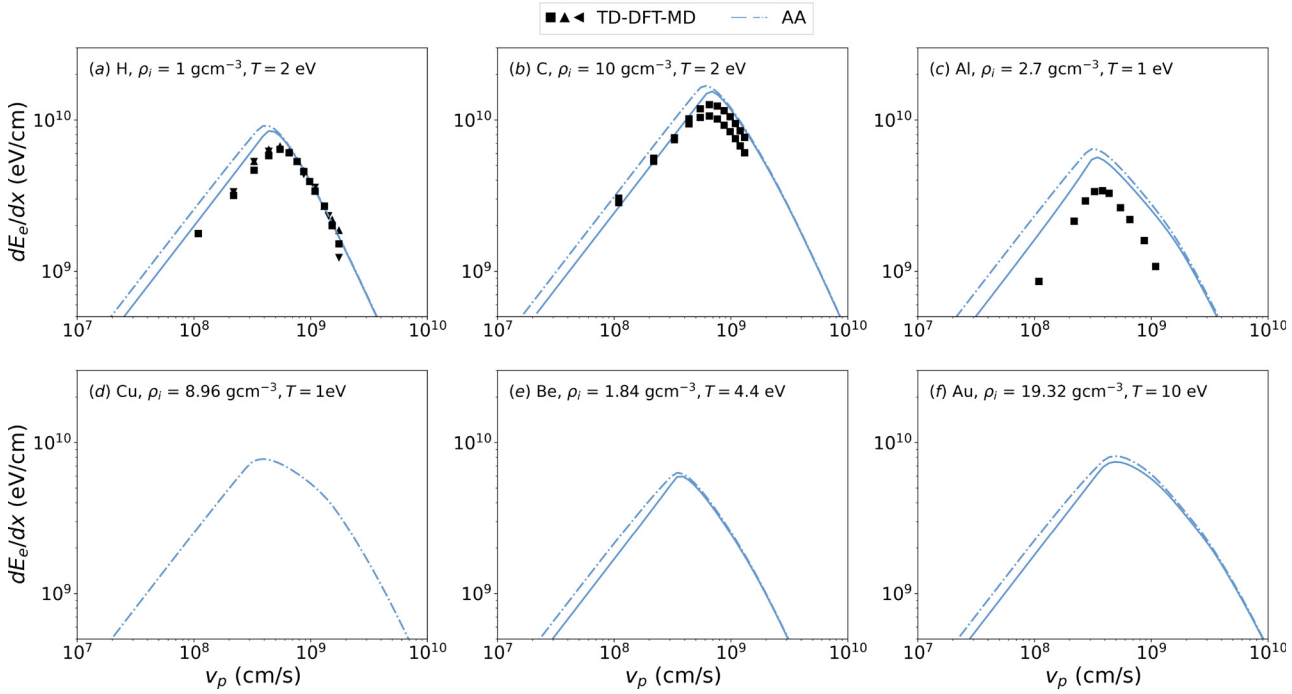

FIG. 12. Electronic contribution to the alpha-particle stopping power for some of the single-species cases in Table I as a function of alpha particle velocity v_p.

costs, these TD-DFT-MD calculations neglected contributions from Al core electrons, which become increasingly significant for fast projectiles[73] and likely explain the discrepancy beyond the stopping power peak, since the AA models do include contributions from core electrons. On the other hand, the local uniform-electron-gas approximation used by the AA models may not accurately capture low-velocity stopping power.[30] Furthermore, the AA models do not account for partial neutralization of the alpha particle as it captures electrons from the plasma—a nonlinear effect beyond the standard Lindhard stopping formula[117] that becomes increasingly important for slow projectiles.

VI. CONCLUSIONS AND FUTURE WORKSHOPS

The results of this workshop have quantified differences between state-of-the-art approaches for computing fundamental material properties of plasmas. Namely, we have compared ionic and electronic transport coefficients, correlation functions, and scalar quantities that characterize the system. Of the data received, we found significant differences between the shear viscosity and thermal conductivity of the ions. For the shear viscosity the difference was at worst *one order of magnitude* between all models and a *factor of six* between similar models. For the ion thermal conductivity, the difference was at worst *one order of magnitude* between all models and a *factor of seven* between similar models.

We also found significant differences in the DC electrical conductivity and electron thermal conductivity—where the difference in the DC electrical conductivity was at worst a *factor of seven* between all models and a *factor of two* between similar models. For the electron thermal conductivity, the difference was at worst *one order of magnitude* between all models and a *factor of five* between similar models. Disagreement was generally larger at lower temperatures and smaller among the most sophisticated DFT-MD models.

In this second iteration of the charged-particle transport coefficient code comparison workshop, we built upon the first workshop by requesting more detailed quantities to characterize the ionic structure, electronic structure, and compare particle trajectories from autocorrelation functions. As a result, additional insight was provided beyond the comparison of integrated quantities; this insight may provide a path forward for improving upon extant models.

Through a comparison with analytic models that estimate transport coefficients within fractions of a second, we have shown the plasma conditions for which these more approximate approaches are viable—primarily in the weakly coupled regime. Additionally, the results of this workshop highlight some of the inherent difficulties in computing transport coefficients—which often constitute cost-benefit tradeoffs of model and statistical accuracy.

In future workshops, we aim to continue exploring disparate plasma conditions relevant to inertial confinement fusion. While the Priority Level System was largely successful in guiding participants to the cases with maximal impact, fewer cases would allow for a more in-depth model comparison, including additional quantities like ion–ion potentials and optical properties (e.g., dynamic conductivities or dielectric functions). In Table IV, we propose a set of six high-priority cases for the next workshop that explore more extreme conditions. We have chosen a single temperature of 3 eV, which remains within reach for multi-atom DFT-based methods. We have also selected higher densities for every element except carbon, whose density remains the same as the present workshop's C1 case as a semi-longitudinal study that will explore the persistence of multi-atom effects on ionic and electronic structure. To facilitate further exploration of mixtures, we have pressure-matched the C, H, and CH cases using an isothermal–isobaric mixing rule, setting the CH molecular volume to the sum of the atomic volumes of the pure C and H cases. The cases of Be, Al, and Cu were chosen to lie along the principal Hugoniot, allowing for access from experimental platforms.

TABLE IV. Suggested cases for the next workshop. For the CH mixture, the ionic number density $n_{species}$ is given in terms of each species, whereas the mass density ρ_{total} is the total mass density of the mixture. We will also request data along these isobars from computationally inexpensive codes.

Element(s)	$n_{species}$ (cm^{-3})	ρ_{total} ($g\,cm^{-3}$)	T (eV)
H	1.8×10^{24}	3	3
C	5.0×10^{23}	10	3
CH	3.9×10^{23}	8.4	3
Be	3.2×10^{23}	4.7	3
Al	1.4×10^{23}	6.4	3
Cu	1.7×10^{23}	18.3	3

Continued efforts to compare transport coefficients predicted by various models will further characterize regimes of accuracy for different approximations, offer insight into underlying physical processes, and inspire improvements to efficient models suitable for tabulating material properties over the wide range of conditions accessed by hydrodynamic simulations. This line of research also helps estimate and reduce uncertainties in transport coefficients, which contribute to uncertainties in hydrodynamic simulations. Ultimately, this work is an important step toward improving the predictive power of large-scale HED simulations of both astrophysical objects and inertial confinement fusion experiments.

ACKNOWLEDGMENTS

We are grateful for the hospitality of the University of California's Livermore Collaboration Center along with the help of A. Cuevas, G. Weiss, C. Bibeau, and A. Mendoza-Olivera. The participants of the workshop included N. Acharya. T. Chuna, P. Efthimion, S. Glenzner, F. Graziani, T. Griffin, T. Haxhimali, F. Kraus, S. Malko, I. Martinez, O. Schilling, J. Shang, and T. White. The authors would like to thank W. Lewis and G. Shipley for helpful feedback and L. Shulenburger for careful proofreading of the manuscript and useful conversations. Sandia National Laboratories is a multi-mission laboratory managed and operated by National Technology and Engineering Solutions of Sandia, LLC, a wholly owned subsidiary of Honeywell International, Inc., for DOE's National Nuclear Security Administration under Contract No. DE-NA0003525. This paper describes objective technical results and analysis. Any subjective views or opinions that might be expressed in the paper do not necessarily represent the views of the U.S. Department of Energy or the United States Government. This work was performed under the auspices of the U.S. Department of Energy by Lawrence Livermore National Laboratory under Contract No. DE-AC52-07NA27344. Los Alamos National Laboratory is managed by Triad National Security, LLC, for the National Nuclear Security Administration of the U.S. Department of Energy

(Contract No. 89233218CNA000001). P.S. and S.K. gratefully acknowledge support from Grant No. DE-NA0004128 funded by the U.S. Department of Energy (DOE), National Nuclear Security Administration (NNSA). L.J.S., J.P.T., C.A.M., A.E.D., R.C.C., K.R.C., M.K.L., A.K., and A.D.B. were supported by the Laboratory Directed Research and Development program (Project Nos. 229428, 230332, and 233196) at Sandia National Laboratories. A.K. and A.D.B. were also partially supported by the U.S. Department of Energy Science Campaign 1. This work was supported in part by NNSA Stewardship Science Academic Programs (DOE Cooperative Agreement No. DE-NA0004146). This material is based upon work supported by the Department of Energy (National Nuclear Security Administration) University of Rochester "National Inertial Confinement Fusion Program" (Award No. DE-NA0004144). This report was prepared as an account of work sponsored by an agency of the U.S. Government. Neither the U.S. Government nor any agency thereof, nor any of their employees, makes any warranty, express or implied, or assumes any legal liability or responsibility for the accuracy, completeness, or usefulness of any information, apparatus, product, or process disclosed, or represents that its use would not infringe privately owned rights. Reference herein to any specific commercial product, process, or service by trade name, trademark, manufacturer, or otherwise does not necessarily constitute or imply its endorsement, recommendation, or favoring by the U.S. Government or any agency thereof. The views and opinions of authors expressed herein do not necessarily state or reflect those of the U.S. Government or any agency thereof. A.J.W., L.A.C., and V.S. were supported by Science Campaign 4 and Laboratory Directed Research and Development of LANL (Project Nos. 20210233ER and 20230322ER). We gratefully acknowledge the support of the Center for Nonlinear Studies (CNLS). This research used computing resources provided by the LANL Institutional Computing and Advanced Scientific Computing programs.

AUTHOR DECLARATIONS

Conflict of Interest

The authors have no conflicts to disclose.

Author Contributions

Lucas James Stanek: Conceptualization (lead); Data curation (lead); Formal analysis (lead); Investigation (lead); Methodology (equal); Supervision (lead); Validation (lead); Visualization (lead); Writing – original draft (lead); Writing – review & editing (lead). **Scott David Baalrud:** Data curation (supporting); Methodology (supporting); Writing – review & editing (supporting). **Lucas Babati:** Data curation (supporting); Methodology (supporting); Writing – review & editing (supporting). **Andrew Baczewski:** Data curation (supporting); Methodology (supporting); Writing – review & editing (supporting). **Mandy Bethkenhagen:** Data curation (supporting); Methodology (supporting); Writing – review & editing (supporting). **Augustin Blanchet:** Data curation (supporting); Methodology (supporting); Writing – review & editing (supporting). **Raymond C. Clay:** Data curation (supporting); Methodology (supporting); Writing – review & editing (supporting). **Kyle R. Cochrane:** Data curation (supporting); Methodology (supporting); Writing – review & editing (supporting). **Lee Collins:** Data curation (supporting); Methodology (supporting); Writing – review & editing (supporting). **Amanda Dumi:** Data curation (supporting); Methodology (supporting); Writing – review & editing (supporting). **Gerald Faussurier:** Data curation (supporting); Methodology (supporting); Writing – review & editing (supporting). **Alina Kononov:** Data curation (equal); Formal analysis (equal); Methodology (equal); Writing – original draft (equal); Writing – review & editing (equal). **Martin French:** Data curation (supporting); Methodology (supporting); Writing – review & editing (supporting). **Zachary A. Johnson:** Data curation (supporting); Methodology (supporting); Writing – review & editing (supporting). **Valentin V. Karasiev:** Data curation (supporting); Methodology (supporting); Writing – review & editing (supporting). **Shashikant Kumar:** Data curation (supporting); Methodology (supporting); Writing – review & editing (supporting). **Meghan K. Lentz:** Data curation (supporting); Methodology (supporting); Writing – review & editing (supporting). **Cody Allen Melton:** Data curation (supporting); Methodology (supporting); Writing – review & editing (supporting). **Katarina A. Nichols:** Data curation (supporting); Methodology (supporting); Writing – review & editing (supporting). **George M. Petrov:** Data curation (supporting); Methodology (supporting); Writing – review & editing (supporting). **Vanina Recoules:** Data curation (supporting); Methodology (supporting); Writing – review & editing (supporting). **Ronald Redmer:** Data curation (supporting); Methodology (supporting); Writing – review & editing (supporting). **Stephanie B. Hansen:** Conceptualization (equal); Data curation (equal); Formal analysis (equal); Investigation (equal); Methodology (equal); Project administration (equal); Supervision (equal); Validation (equal); Writing – original draft (equal); Writing – review & editing (equal). **Gerd Roepke:** Data curation (supporting); Methodology (supporting); Writing – review & editing (supporting). **Maximilian Schörner:** Data curation (supporting); Methodology (supporting); Writing – review & editing (supporting). **Nathaniel R. Shaffer:** Data curation (supporting); Methodology (supporting); Writing – review & editing (supporting). **Vidushi Sharma:** Data curation (supporting); Methodology (supporting); Writing – review & editing (supporting). **Luciano Germano Silvestri:** Data curation (supporting); Methodology (supporting); Writing – review & editing (supporting). **François Soubiran:** Data curation (supporting); Methodology (supporting); Writing – review & editing (supporting). **Phanish Suryanarayana:** Data curation (supporting); Methodology (supporting); Writing – review & editing (supporting). **Mikael Tacu:** Data curation (supporting); Methodology (supporting); Writing – review & editing (supporting). **Joshua Townsend:** Data curation (supporting); Methodology (supporting); Writing – review & editing (supporting). **Alexander James White:** Data curation (supporting); Methodology (supporting); Writing – review & editing (supporting). **Brian Michael Haines:** Conceptualization (equal); Supervision (equal); Writing – review & editing (supporting). **Suxing Hu:** Conceptualization (equal); Data curation (supporting); Supervision (equal); Writing – review & editing (supporting). **Patrick Francis Knapp:** Conceptualization (equal); Supervision (equal); Writing – review & editing (supporting). **Michael S. Murillo:** Conceptualization (equal); Data curation (supporting); Methodology (equal); Supervision (equal); Validation (supporting); Writing – review & editing (equal). **Liam Stanton:** Conceptualization (equal); Project administration (supporting); Writing – review & editing (supporting). **Heather D. Whitley:** Conceptualization (equal); Funding acquisition (equal); Project administration (lead); Resources (equal); Supervision (equal); Writing – review & editing (supporting).

TABLE V. Computed transport coefficients for plasma conditions detailed in Table I. For brevity, entries in the Case ID/Submitter column have been labeled by a single submitter determined by how the data were received; please refer to Table II for a full list of the collaborations and institutions. Exchange-correlation functionals used include LDA,[118] PBE,[119] and Tr^{2}SCANL.[120] Kubo–Greenwood calculations marked with (∗) were performed with employment of the thermal hybrid KDT0 XC functional[121] on top of the Tr^{2}SCANL snapshots (see further details in Ref. 122).

Case ID/Submitter	$\sigma\left(\frac{1}{\Omega\,\mathrm{cm}}10^4\right)$	$\kappa_e\left(\frac{\mathrm{erg}}{\mathrm{s\,cm\,K}}10^7\right)$	$\eta\left(\frac{\mathrm{g}}{\mathrm{cm\,s}}10^{-3}\right)$	$\kappa_i\left(\frac{\mathrm{erg}}{\mathrm{s\,cm\,K}}10^7\right)$	$g\left(\frac{\mathrm{erg}}{\mathrm{cm^3K}}10^{20}\right)$	XC	Model
H1 (1 g cm^{-3}, 2 eV)							
L. Babati	⋯	⋯	7.88	0.24	⋯	LDA	KT
G. Faussurier	1.47	8.03	⋯	⋯	11.81	LDA	AA
M. French	1.29 ± 0.03	7.5 ± 0.15	⋯	⋯	⋯	PBE	DFT-MD
M. French	1.05 ± 0.02	6.4 ± 0.13	⋯	⋯	⋯	HSE	DFT-MD
S. Hansen	$1^{+1.50}_{-0.42}$	$7^{+7.69}_{-2.14}$	⋯	⋯	10.23 ± 1.12	LDA	AA
S. Hu	1.4 ± 0.10	7.5 ± 0.31	11.48	⋯	⋯	PBE	DFT-MD
S. Hu	1.25 ± 0.08	6.7 ± 0.26	13.36	⋯	⋯	TSCANL	DFT-MD
N. Shaffer	2.01	9.61	⋯	⋯	11.17	LDA	KT
V. Sharma	1.4 ± 0.15	7.2 ± 0.41	⋯	⋯	⋯	PBE	DFT-MD
L. Silvestri	⋯	⋯	7.0 ± 0.03	0.845 ± 0.004	⋯	LDA	MD
F. Soubiran	1.31 ± 0.04	7.58 ± 0.01	11 ± 4.00	⋯	⋯	PBE	DFT-MD
L. Stanek	⋯	⋯	12 ± 3.18	0.5 ± 0.11	⋯	LDA	MD
P. Suryanarayana	⋯	⋯	12 ± 0.91	0.168 ± 0.002	⋯	LDA	DFT-MD
J. Townsend	1.4 ± 0.004	8.05 ± 0.01	8 ± 1.64	⋯	⋯	LDA	DFT-MD
C1 (10 g cm^{-3}, 2 eV)							
L. Babati	⋯	⋯	5.80	0.015	⋯	LDA	KT
M. Bethkenhagen	1.63 ± 0.03	9 ± 0.18	⋯	⋯	⋯	PBE	DFT-MD
G. Faussurier	1.14	6.44	⋯	⋯	10.55	LDA	AA
S. Hansen	$1^{+1.06}_{-0.36}$	$6^{+5.99}_{-2.02}$	⋯	⋯	8 ± 3.52	LDA	AA
V. Karasiev	1.69 ± 0.06	9.5 ± 0.16	⋯	⋯	⋯	PBE	DFT-MD
V. Karasiev	1.04 ± 0.06	6.9 ± 0.28	⋯	⋯	⋯	Tr^{2}SCANL*	DFT-MD
C. Melton	1.60 ± 0.01	8.80	28.2 ± 0.3	⋯	⋯	LDA	DFT-MD
N. Shaffer	1.87	9.39	⋯	⋯	11.40	LDA	KT
V. Sharma	1.26 ± 0.06	7.7 ± 0.24	⋯	⋯	⋯	PBE	DFT-MD
L. Silvestri	⋯	⋯	104 ± 0.5	0.942 ± 0.005	⋯	LDA	MD
F. Soubiran	1.58 ± 0.04	8.8 ± 0.15	32 ± 21.00	⋯	⋯	PBE	DFT-MD
L. Stanek	⋯	⋯	64 ± 14.57	0.14 ± 0.04	⋯	LDA	MD
P. Suryanarayana	⋯	⋯	29 ± 1.61	1.02 ± 0.02	⋯	LDA	DFT-MD
CH1 (1 g cm^{-3}, 2 eV)							
M. Bethkenhagen	0.174 ± 0.003	0.71 ± 0.02	⋯	⋯	⋯	PBE	DFT-MD
R. Clay	0.168 ± 0.004	0.72 ± 0.01	6.5 ± 0.9	⋯	⋯	LDA	DFT-MD
V. Karasiev	0.19 ± 0.03	0.80 ± 0.06	⋯	⋯	⋯	PBE	DFT-MD
V. Karasiev	0.14 ± 0.02	0.74 ± 0.05	⋯	⋯	⋯	TSCANL*	DFT-MD
V. Sharma	0.188 ± 0.009	0.78 ± 0.02	⋯	⋯	⋯	PBE	DFT-MD
F. Soubiran	0.18 ± 0.02	0.67 ± 0.02	8 ± 3.2	⋯	⋯	PBE	DFT-MD
Al1 (2.7 g cm^{-3}, 1 eV)							
L. Babati	⋯	⋯	1.51	0.0018	⋯	LDA	KT
A. Dumi	2.461 ± 0.004	1.45 ± 0.02	4 ± 0.82	⋯	⋯	LDA	DFT-MD
G. Faussurier	4.18	11.5	⋯	⋯	0.0218	LDA	AA
S. Hansen	$4^{+2.25}_{-1.30}$	$7^{+4.06}_{-2.36}$	⋯	⋯	0.016 ± 0.002	LDA	AA
V. Karasiev	2.03 ± 0.05	5.69 ± 0.15	⋯	⋯	⋯	PBE	DFT-MD
V. Karasiev	1.38 ± 0.08	4.75 ± 0.22	⋯	⋯	⋯	TSCANL*	DFT-MD
G. Petrov	5.65	15.3	⋯	⋯	0.0101	LDA	AA

TABLE V. (*Continued.*)

Case ID/Submitter	$\sigma\left(\frac{1}{\Omega\,\mathrm{cm}}10^4\right)$	$\kappa_e\left(\frac{\mathrm{erg}}{\mathrm{s\,cm\,K}}10^7\right)$	$\eta\left(\frac{\mathrm{g}}{\mathrm{cm\,s}}10^{-3}\right)$	$\kappa_i\left(\frac{\mathrm{erg}}{\mathrm{s\,cm\,K}}10^7\right)$	$g\left(\frac{\mathrm{erg}}{\mathrm{cm^3K}}10^{20}\right)$	XC	Model
M. Schörner	2.6 ± 0.13	7.33 ± 0.53	⋯	⋯	⋯	PBE	DFT-MD
N. Shaffer	2.15	4.09	⋯	⋯	0.036	LDA	KT
V. Sharma	2.38 ± 0.07	6.46 ± 0.19	⋯	⋯	⋯	PBE	DFT-MD
L. Silvestri	⋯	⋯	7.25 ± 0.04	0.0436 ± 0.0002	⋯	LDA	MD
F. Soubiran	2.44 ± 0.03	6.8 ± 0.01	8 ± 4.40	⋯	⋯	GGA	DFT-MD
L. Stanek	⋯	⋯	8 ± 3.13	0.014 ± 0.003	⋯	LDA	MD

TABLE VI. Computed transport coefficients for plasma conditions detailed in Table I. For brevity, entries in the Case ID/Submitter column have been labeled by a single submitter determined by how the data were received; please refer to Table II for a full list of the collaborations and institutions. Note that (ext)-DFT-MD denotes that extended DFT-MD was used—see Ref. 42 for details. Also note that (mix)-DFT-MD denotes that mixed stochastic-deterministic DFT-MD was used—see Ref. 43.

Case ID/Submitter	$\sigma\left(\frac{1}{\Omega\,\mathrm{cm}}10^4\right)$	$\kappa_e\left(\frac{\mathrm{erg}}{\mathrm{s\,cm\,K}}10^7\right)$	$\eta\left(\frac{\mathrm{g}}{\mathrm{cm\,s}}10^{-3}\right)$	$\kappa_i\left(\frac{\mathrm{erg}}{\mathrm{s\,cm\,K}}10^7\right)$	$g\left(\frac{\mathrm{erg}}{\mathrm{cm^3K}}10^{20}\right)$	XC	Model
Cu1 ($8.96\,\mathrm{g\,cm^{-3}}$, 1 eV)							
K. Cochrane	2	4.25	14 ± 0.5	⋯	⋯	PBE	DFT-MD
G. Faussurier	2.75	7.62	⋯	⋯	0.0133	LDA	AA
S. Hansen	$6^{+32.20}_{-2.70}$	$10^{+55.93}_{-4.68}$	⋯	⋯	0.01 ± 0.015	LDA	AA
S. Hu	0.90 ± 0.02	2.50 ± 0.03	16.87	⋯	⋯	PBE	DFT-MD
S. Hu	1.20 ± 0.01	3.75 ± 0.08	16.42	⋯	⋯	TSCANL	DFT-MD
G. Petrov	3.13	18.5	⋯	⋯	0.0116	LDA	AA
F. Soubiran	1.80 ± 0.02	3.90 ± 0.03	19 ± 8.00	⋯	⋯	LDA	DFT-MD
L. Stanek	⋯	⋯	19 ± 5.76	0.013 ± 0.003	⋯	LDA	MD
HCu1 ($1.8\,\mathrm{g\,cm^{-3}}$, 1 eV)							
S. Hu	0.09 ± 0.008	0.332 ± 0.023	0.796	⋯	⋯	PBE	DFT-MD
S. Hu	0.11 ± 0.004	0.463 ± 0.005	5.135	⋯	⋯	TSCANL	DFT-MD
M. Lentz	0.09 ± 0.002	0.39 ± 0.007	1.8 ± 0.58	⋯	⋯	LDA	DFT-MD
Be1 ($1.84\,\mathrm{g\,cm^{-3}}$, 4.4 eV)							
L. Babati	⋯	⋯	8.81	0.031	⋯	LDA	KT
G. Faussurier	0.83	8.01	⋯	⋯	0.470	LDA	AA
S. Hansen	$0.6^{+0.23}_{-0.04}$	$5.55^{+2.16}_{-0.34}$	⋯	⋯	0.4 ± 0.14	LDA	AA
S. Hu	0.65 ± 0.02	7.2 ± 0.11	12.84	⋯	⋯	PBE	DFT-MD
S. Hu	0.65 ± 0.03	7.4 ± 0.18	6.33	⋯	⋯	TSCANL	DFT-MD
M. Schörner	0.66 ± 0.01	7.3 ± 0.17	⋯	⋯	⋯	PBE	DFT-MD
N. Shaffer	0.81	9.62	⋯	⋯	0.749	LDA	KT
V. Sharma	0.58 ± 0.01	6.3 ± 0.11	⋯	⋯	⋯	PBE	DFT-MD
V. Sharma	0.57 ± 0.01	6.1 ± 0.27	⋯	⋯	⋯	PBE	(mix)-DFT-MD
L. Stanek	⋯	⋯	11 ± 2.21	0.06 ± 0.015	⋯	LDA	MD
CH2 ($0.9\,\mathrm{g\,cm^{-3}}$, 7.8 eV)							
L. Babati	⋯	⋯	8.61	0.0257	⋯	LDA	KT
N. Shaffer	⋯	⋯	⋯	⋯	1.72	LDA	KT
V. Sharma	0.23 ± 0.010	7.38 ± 0.24	⋯	⋯	⋯	PBE	DFT-MD
V. Sharma	0.23 ± 0.015	7.52 ± 0.69	⋯	⋯	⋯	PBE	(mix)-DFT-MD
F. Soubiran	0.21 ± 0.002	6.5 ± 0.1	15.00	⋯	⋯	PBE	(ext)-DFT-MD

TABLE VI. (*Continued.*)

Case ID/Submitter	$\sigma\left(\frac{1}{\Omega\,\mathrm{cm}}10^4\right)$	$\kappa_e\left(\frac{\mathrm{erg}}{\mathrm{s\,cm\,K}}10^7\right)$	$\eta\left(\frac{\mathrm{g}}{\mathrm{cm\,s}}10^{-3}\right)$	$\kappa_i\left(\frac{\mathrm{erg}}{\mathrm{s\,cm\,K}}10^7\right)$	$g\left(\frac{\mathrm{erg}}{\mathrm{cm^3K}}10^{20}\right)$	XC	Model
Au1 (19.32 g cm^{-3}, 10 eV)							
L. Babati	···	···	24.98	0.0040	···	LDA	KT
G. Faussurier	1.07	22.8	···	···	0.026	LDA	AA
S. Hansen	$0.73^{+0.001}_{-0.067}$	$15.50^{+0.01}_{-1.45}$	···	···	0.024 ± 0.0072	LDA	AA
S. Hu	1.07 ± 0.03	26.2 ± 0.3	44 ± 1.00	···	···	TSCANL	DFT-MD
V. Karasiev	0.99 ± 0.02	24.7 ± 0.3	···	···	···	TSCANL	DFT-MD
N. Shaffer	1.18	28.3	···	···	0.036	LDA	KT
F. Soubiran	1.024 ± 0.001	27.34 ± 0.03	51 ± 1.00	···	···	LDA	(ext)-DFT-MD
L. Stanek	···	···	42 ± 12.04	0.011 ± 0.003	···	LDA	MD
H3 (10 g cm^{-3}, 20 eV)							
L. Babati	···	···	209.9	0.651	···	LDA	KT
G. Faussurier	23.8	1206.0	···	···	87.3	LDA	AA
S. Hansen	24.7	730.9	···	···	···	LDA	AA
N. Shaffer	17.8	867	···	···	129	LDA	KT
V. Sharma	12 ± 1.58	757 ± 80.4	···	···	···	PBE	DFT-MD
M. Bethkenhagen	14.8 ± 0.6	850.0 ± 34.0	···	···	···	PBE	DFT-MD

TABLE VII. Submitted data for the electronic contribution to the alpha-particle stopping power. The column denoted "peak position" gives the alpha particle velocity that corresponds to the largest stopping power—denoted as "peak height." The computation time reported denotes the total simulation time. For example, the total computation time for a TD-DFT-MD simulation is determined from $t_{\mathrm{total}} = \sum_p t_{p,\mathrm{sim}} N_{p,\mathrm{CPUs}}$, where p is the number of projectiles simulated (i.e., the number of alpha particle velocities for a case), $t_{p,\mathrm{sim}}$ is the duration of the simulation for projectile p, and $N_{p,\mathrm{CPUs}}$ is the number of CPU-cores used for the simulation of projectile p. Note that (mix)-TD-DFT-MD denotes that mixed stochastic-deterministic TD-DFT-MD was used—see Ref. 43.

Case ID/Submitter	Peak position (cm/s)	Peak height (eV/cm)	XC	Model	Computation time (s)
H1 (1 g cm^{-3}, 2 eV)					
G. Faussurier	4.38×10^8	9.13×10^9	LDA	AA	1.7×10^2
S. Hansen	4.90×10^8	8.36×10^9	LDA	AA	···
A. Kononov	5.47×10^8	6.39×10^9	LDA	TD-DFT-MD	3.8×10^8
K. Nichols	4.38×10^8	6.21×10^9	PBE	TD-DFT-MD	1.5×10^8
A. White	5.47×10^8	6.68×10^9	PBE	(mix)-TD-DFT-MD	1.7×10^9
C1 (10 g cm^{-3}, 2 eV)					
G. Faussurier	6.19×10^8	1.68×10^{10}	LDA	AA	1.9×10^2
S. Hansen	6.92×10^8	1.54×10^{10}	LDA	AA	···
A. Kononov	6.56×10^8	1.26×10^{10}	LDA[a]	TD-DFT-MD	5.2×10^6
A. Kononov	6.56×10^8	1.06×10^{10}	LDA[b]	TD-DFT-MD	9.6×10^7
CH1 (1 g cm^{-3}, 2 eV)					
A. Kononov	4.38×10^8	2.32×10^9	LDA	TD-DFT-MD	2.4×10^8
Al1 (2.7 g cm^{-3}, 1 eV)					
G. Faussurier	3.10×10^8	6.43×10^9	LDA	AA	1.1×10^2
S. Hansen	3.47×10^8	5.66×10^9	LDA	AA	···
A. Kononov	3.83×10^8	3.40×10^9	LDA	TD-DFT-MD	5.2×10^9
Cu1 (8.96 g cm^{-3}, 1 eV)					
G. Faussurier	3.90×10^8	7.78×10^9	LDA	AA	6.4×10^2
Be1 (1.84 g cm^{-3}, 4.4 eV)					
G. Faussurier	3.48×10^8	6.32×10^9	LDA	AA	2.3×10^2

TABLE VII. (*Continued.*)

Case ID/Submitter	Peak position (cm/s)	Peak height (eV/cm)	XC	Model	Computation time (s)
S. Hansen	3.89×10^{8}	5.96×10^{9}	LDA	AA	···
Au1 (19.32 g cm^{-3}, 10 eV)					
G. Faussurier	4.92×10^{8}	8.13×10^{9}	LDA	AA	2.4×10^{2}
S. Hansen	4.90×10^{8}	7.45×10^{9}	LDA	AA	···
H3 (10 g cm^{-3}, 20 eV)					
G. Faussurier	8.74×10^{8}	2.57×10^{10}	LDA	AA	2.3×10^{2}
S. Hansen	9.78×10^{8}	2.38×10^{10}	LDA	AA	···

[a]For this case all-electron calculations with bare Coulomb potentials were carried out.
[b]For this case pseudopotentials were employed with 4 valence electrons per C ion.

TABLE VIII. Computed total pressure for plasma conditions detailed in Table I. For brevity, entries in the Case ID/Submitter column have been labeled by a single submitter determined by how the data were received; see Table II for a full list of the collaborations and institutions. Note that (ext)-DFT-MD denotes that extended DFT-MD was used–see Ref. 42 for details.

Case ID/Submitter	P_{total} (Mbar)	XC	Model
H1 (1 g cm^{-3}, 2 eV)			
G. Faussurier	6.70	LDA	AA
M. French	4.81	PBE	DFT-MD
M. French	4.75	HSE	DFT-MD
S. Hansen	5.46	LDA	AA
S. Hu	4.82 ± 0.07	PBE	DFT-MD
S. Hu	4.81 ± 0.06	TSCANL	DFT-MD
P. Suryanarayana	4.79 ± 0.01	LDA	DFT-MD
F. Soubiran	4.82	PBE	DFT-MD
J. Townsend	4.73 ± 0.004	LDA	DFT-MD
C1 (10 g cm^{-3}, 2 eV)			
M. Bethkenhagen	28.6	PBE	DFT-MD
G. Faussurier	43.5	LDA	AA
S. Hansen	34.7	LDA	AA
V. Karasiev	28.5	PBE	DFT-MD
V. Karasiev	28.7	Tr^{2}SCANL	DFT-MD
C. Melton	28.1	LDA	DFT-MD
P. Suryanarayana	28.93 ± 0.02	LDA	DFT-MD
F. Soubiran	28.5 ± 0.002	PBE	DFT-MD
CH1 (1 g cm^{-3}, 2 eV)			
M. Bethkenhagen	0.370	PBE	DFT-MD
R. Clay	0.338	LDA	DFT-MD
V. Karasiev	0.370	PBE	DFT-MD
V. Karasiev	0.330	TSCANL	DFT-MD
F. Soubiran	0.368 ± 0.001	PBE	DFT-MD
Al1 (2.7 g cm^{-3}, 1 eV)			
A. Dumi	0.513 ± 0.001	LDA	DFT-MD
G. Faussurier	1.01	LDA	AA

TABLE VIII. (*Continued.*)

Case ID/Submitter	P_{total} (Mbar)	XC	Model
S. Hansen	0.808	LDA	AA
V. Karasiev	0.443	PBE	DFT-MD
V. Karasiev	0.425	TSCANL	DFT-MD
M. Schörner	0.441 ± 0.001	PBE	DFT-MD
F. Soubiran	0.440 ± 0.001	GGA	DFT-MD
Cu1 (8.96 g cm^{-3}, 1 eV)			
K. Cochrane	0.766	PBE	DFT-MD
G. Faussurier	1.67	LDA	AA
S. Hansen	1.04	LDA	AA
S. Hu	0.377 ± 0.053	PBE	DFT-MD
S. Hu	0.340 ± 0.053	TSCANL	DFT-MD
F. Soubiran	0.651 ± 0.003	LDA	DFT-MD
HCu1 (1.8 g cm^{-3}, 1 eV)			
S. Hu	0.02 ± 0.0158	PBE	DFT-MD
S. Hu	0.01 ± 0.0139	TSCANL	DFT-MD
M. Lentz	0.0311 ± 0.0001	LDA	DFT-MD
Be1 (1.84 g cm^{-3}, 4.4 eV)			
G. Faussurier	3.10	LDA	AA
S. Hansen	2.78	LDA	AA
S. Hu	2.36 ± 0.04	PBE	DFT-MD
S. Hu	2.29 ± 0.04	TSCANL	DFT-MD
M. Schörner	2.37 ± 0.003	PBE	DFT-MD
CH2 (0.9 g cm^{-3}, 7.8 eV)			
F. Soubiran	2.04 ± 0.002	PBE	(ext)-DFT-MD
Au1 (19.32 g cm^{-3}, 10 eV)			
G. Faussurier	6.09	LDA	AA
S. Hansen	6.51	LDA	AA
S. Hu	5.87 ± 0.2	TSCANL	DFT-MD
V. Karasiev	5.76	TSCANL	DFT-MD
F. Soubiran	6.01 ± 0.01	LDA	(ext)-DFT-MD

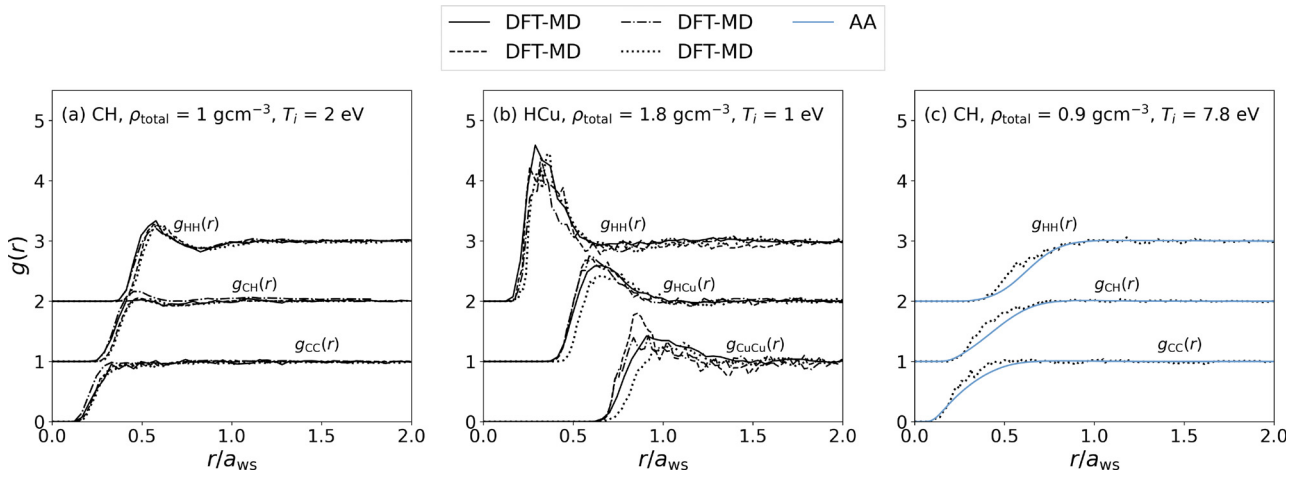

FIG. 13. Ionic radial distribution function, $g(r)$, for the mixture cases in Table I. $g(r)$s from AA models are obtained by solving the quantum Ornstein–Zernike equations and employing the hyper-netted chain approximation while $g(r)$s obtained from DFT-MD models are obtained directly from ensemble-averaged particle positions. Note that the $g(r)$s for each pair of species have been shifted vertically for visual clarity.

TABLE IX. Additional DC electrical conductivity and shear viscosity data for hydrogen. For brevity, entries in the Case ID/Submitter column have been labeled by a single submitter determined by how the data were received; see Table II for a full list of the collaborations and institutions.

Case/Submitter	T (eV)	$\sigma\left(\frac{1}{\Omega\,\mathrm{cm}}10^4\right)$	$\eta\left(\frac{\mathrm{g}}{\mathrm{cm\,s}}\right)$	XC	Model
H (1 g cm^{-3})					
G. Röpke	70	7.75	···	···	Analytic
G. Röpke	100	10.7	···	···	Analytic
G. Röpke	200	21.9	···	···	Analytic
G. Röpke	400	48.3	···	···	Analytic
G. Röpke	700	95.1	···	···	Analytic
G. Röpke	1000	148	···	···	Analytic
H (1.67 g cm^{-3})					
L. Babati	2	···	0.00901	LDA	KT
L. Babati	5	···	0.0233	LDA	KT
L. Babati	8	···	0.0396	LDA	KT
L. Babati	10	···	0.0513	LDA	KT
L. Babati	20	···	0.124	LDA	KT
P. Suryanarayana	43.1	···	1.0 ± 0.17	LDA	DFT-MD
L. Babati	50	···	0.491	LDA	KT
P. Suryanarayana	64.6	···	2.0 ± 0.2	LDA	DFT-MD
L. Babati	80	···	1.11	LDA	KT
P. Suryanarayana	86.2	···	3.1 ± 0.3	LDA	DFT-MD
L. Babati	100	···	1.67	LDA	KT
G. Röpke	100	13 ± 0.25	···	···	Analytic
P. Suryanarayana	107.7	···	4.5 ± 0.5	LDA	DFT-MD
P. Suryanarayana	129.3	···	6.1 ± 0.7	LDA	DFT-MD
L. Babati	200	···	6.43	LDA	KT
L. Babati	500	···	43.4	LDA	KT
L. Babati	800	···	121	LDA	KT
L. Babati	1000	···	197	LDA	KT
G. Röpke	1000	159 ± 3.2	···	···	Analytic
G. Röpke	10 000	3130 ± 60	···	···	Analytic
G. Röpke	20 000	7950 ± 160	···	···	Analytic
H (10 g cm^{-3})					
L. Babati	8	···	0.0715	LDA	KT
N. Shaffer	8	22.1	···	LDA	KT
L. Babati	10	···	0.0912	LDA	KT
N. Shaffer	10	20.8	···	LDA	KT
L. Babati	20	···	0.210	LDA	KT
N. Shaffer	20	17.8	···	LDA	KT
L. Babati	50	···	0.776	LDA	KT
N. Shaffer	50	18.4	···	LDA	KT
L. Babati	80	···	1.66	LDA	KT
N. Shaffer	80	21.6	···	LDA	KT
L. Babati	100	···	2.44	LDA	KT
G. Röpke	100	26.6 ± 0.5	···	···	Analytic
N. Shaffer	100	23.7	···	LDA	KT
L. Babati	200	···	8.74	LDA	KT
N. Shaffer	200	33.9	···	LDA	KT
L. Babati	500	···	54.7	LDA	KT
N. Shaffer	500	87.1	···	LDA	KT
L. Babati	800	···	147	LDA	KT
N. Shaffer	800	148.9	···	LDA	KT
L. Babati	1000	···	238	LDA	KT
G. Röpke	1000	207 ± 4	···	···	Analytic

TABLE IX. (*Continued.*)

Case/Submitter	T (eV)	$\sigma\left(\frac{1}{\Omega\,\mathrm{cm}}10^4\right)$	$\eta\left(\frac{\mathrm{g}}{\mathrm{cm\,s}}\right)$	XC	Model
N. Shaffer	1000	193.8	⋯	LDA	KT
H (100 g cm^{-3})					
L. Babati	50	⋯	1.49	LDA	KT
N. Shaffer	50	182	⋯	LDA	KT
L. Babati	80	⋯	2.92	LDA	KT
N. Shaffer	80	159	⋯	LDA	KT
L. Babati	100	⋯	4.14	LDA	KT
N. Shaffer	100	153	⋯	LDA	KT
L. Babati	200	⋯	13.5	LDA	KT
N. Shaffer	200	153	⋯	LDA	KT
L. Babati	500	⋯	77.4	LDA	KT
N. Shaffer	500	213	⋯	LDA	KT
L. Babati	800	⋯	200	LDA	KT
N. Shaffer	800	269	⋯	LDA	KT
L. Babati	1000	⋯	317	LDA	KT
G. Röpke	1000	340 ± 7	⋯	⋯	Analytic
N. Shaffer	1000	320	⋯	LDA	KT

DATA AVAILABILITY

The data that support the findings of this study are available from the corresponding author upon reasonable request.

APPENDIX: ADDITIONAL DATA

Due to the quantity of the received data, not all data were suitable for a broad comparison between models. In this section, we present additional data that participants submitted. These data include the total pressure for the cases given in Table I, which is displayed in Table VIII. The DC electrical conductivity and shear viscosity for hydrogen at various densities are also provided in Table IX. Finally, we display $g(r)$s for the mixture cases of Table I in Fig. 13.

REFERENCES

[1]N. B. Volkov and A. I. Lipchak, "Thermodynamic functions of a metal exposed to high energy densities in compressed and expanded states," Condens. Matter **7**(4), 61 (2022).
[2]N. B. Volkov and A. I. Lipchak, "The transport and optical characteristics of a metal exposed to high-density energy fluxes in compressed and expanded states of matter," Condens. Matter **8**(3), 70 (2023).
[3]P. E. Grabowski, S. B. Hansen, M. S. Murillo, L. G. Stanton, F. R. Graziani, A. B. Zylstra, S. D. Baalrud, P. Arnault, A. D. Baczewski, L. X. Benedict *et al.*, "Review of the first charged-particle transport coefficient comparison workshop," High Energy Density Phys. **37**, 100905 (2020).
[4]L. J. Stanek, S. D. Bopardikar, and M. S. Murillo, "Multifidelity regression of sparse plasma transport data available in disparate physical regimes," Phys. Rev. E **104**(6), 065303 (2021).
[5]M. S. Murillo, "Data-driven electrical conductivities of dense plasmas," Front. Phys. **10**, 867990 (2022).
[6]R. L. Liboff, *Kinetic Theory: Classical, Quantum, and Relativistic Descriptions* (Springer Science & Business Media, 2003).
[7]J. I. Castor, *Radiation Hydrodynamics* (Cambridge University Press, 2004).
[8]R. Paul Drake, "High-energy-density physics," Phys. Today **63**(6), 28–33 (2010).
[9]N. B. Volkov, E. A. Chingina, and A. P. Yalovets, "Dynamical equations and transport coefficients for the metals at high pulse electromagnetic fields," J. Phys.: Conf. Ser. **774**, 012147 (2016).
[10]L. J. Stanek, B. M. Haines, S. B. Hansen, S. X. Hu, P. F. Knapp, M. S. Murillo, L. G. Stanton, and H. D. Whitley, "Community call for the second charged-particle transport coefficient code comparison workshop," (unpublished).
[11]L. G. Stanton and M. S. Murillo, "Efficient model for electronic transport in high energy-density matter," Phys. Plasmas **28**(8), 082301 (2021).
[12]G. Röpke, M. Schörner, R. Redmer, and M. Bethkenhagen, "Virial expansion of the electrical conductivity of hydrogen plasmas," Phys. Rev. E **104**(4), 045204 (2021).
[13]G. Röpke, "Electrical conductivity of hydrogen plasmas: Low-density benchmarks and virial expansion including e – e collisions," Phys. Plasmas **31**, 042301 (2024).
[14]M. P. Desjarlais, "Practical improvements to the Lee-More conductivity near the metal-insulator transition," Contributions to Plasma Phys. **41**(2–3), 267–270 (2001).
[15]M. S. Murillo, "Viscosity estimates for strongly coupled Yukawa systems," Phys. Rev. E **62**(3), 4115 (2000).
[16]M. S. Murillo, "Viscosity estimates of liquid metals and warm dense matter using the Yukawa reference system," High Energy Density Phys. **4**(1–2), 49–57 (2008).
[17]L. G. Stanton and M. S. Murillo, "Ionic transport in high-energy-density matter," Phys. Rev. E **93**(4), 043203 (2016).
[18]S. D. Baalrud and J. Daligault, "Effective potential theory for transport coefficients across coupling regimes," Phys. Rev. Lett. **110**(23), 235001 (2013).
[19]J. Daligault, S. D. Baalrud, C. E. Starrett, D. Saumon, and T. Sjostrom, "Ionic transport coefficients of dense plasmas without molecular dynamics," Phys. Rev. Lett. **116**(7), 075002 (2016).
[20]S. D. Baalrud and J. Daligault, "Mean force kinetic theory: A convergent kinetic theory for weakly and strongly coupled plasmas," Phys. Plasmas **26**(8), 082106 (2019).
[21]C. E. Starrett and D. Saumon, "Fully variational average atom model with ion-ion correlations," Phys. Rev. E **85**, 026403 (2012).
[22]V. V. Karasiev, T. Sjostrom, J. Dufty, and S. B. Trickey, "Accurate homogeneous electron gas exchange-correlation free energy for local spin-density calculations," Phys. Rev. Lett. **112**, 076403 (2014).
[23]N. R. Shaffer and C. E. Starrett, "Model of electron transport in dense plasmas spanning temperature regimes," Phys. Rev. E **101**(5), 053204 (2020).
[24]G. Faussurier and C. Blancard, "Friedel sum rule at finite temperature in hot dense plasmas," Phys. Plasmas **28**(4), 042710 (2021).
[25]G. Faussurier, "Electron-ion coupling factor for temperature relaxation in dense plasmas," Phys. Rev. E **101**(2), 023206 (2020).
[26]G. Faussurier and C. Blancard, "Resistivity saturation in warm dense matter," Phys. Rev. E **91**(1), 013105 (2015).
[27]G. Faussurier, C. Blancard, P. Cossé, and P. Renaudin, "Equation of state, transport coefficients, and stopping power of dense plasmas from the average-atom model self-consistent approach for astrophysical and laboratory plasmas," Phys. Plasmas **17**(5), 052707 (2010).
[28]S. B. Hansen, A. Y. Faenov, T. A. Pikuz, K. B. Fournier, R. Shepherd, H. Chen, K. Widmann, S. C. Wilks, Y. Ping, H. K. Chung *et al.*, "Temperature determination using K α spectra from M-shell Ti ions," Phys. Rev. E **72**(3), 036408 (2005).
[29]P. A. Sterne, S. B. Hansen, B. G. Wilson, and W. A. Isaacs, "Equation of state, occupation probabilities and conductivities in the average atom Purgatorio code," High Energy Density Phys. **3**(1), 278–282 (2007).
[30]T. W. Hentschel, A. Kononov, A. Olmstead, A. Cangi, A. D. Baczewski, and S. B. Hansen, "Improving dynamic collision frequencies: Impacts on dynamic structure factors and stopping powers in warm dense matter," Phys. Plasmas **30**(6), 062703 (2023).
[31]G. M. Petrov, A. Davidson, D. Gordon, and J. Peñano, "Modeling of short-pulse laser-metal interactions in the warm dense matter regime using the two-temperature model," Phys. Rev. E **103**(3), 033204 (2021).
[32]Z. A. Johnson, L. G. Silvestri, G. M. Petrov, L. G. Stanton, and M. S. Murillo, "Comparison of transport models in dense plasmas," Phys. Plasmas (submitted) (2024).

[33]L. G. Silvestri, L. J. Stanek, G. Dharuman, Y. Choi, and M. S. Murillo, "Sarkas: A fast pure-python molecular dynamics suite for plasma physics," Comput. Phys. Commun. **272**, 108245 (2022).
[34]A. P. Thompson, H. M. Aktulga, R. Berger, D. S. Bolintineanu, W. M. Brown, P. S. Crozier, P. J. in 't Veld, A. Kohlmeyer, S. G. Moore, T. D. Nguyen, R. Shan, M. J. Stevens, J. Tranchida, C. Trott, and S. J. Plimpton, "LAMMPS - A flexible simulation tool for particle-based materials modeling at the atomic, meso, and continuum scales," Comp. Phys. Commun. **271**, 108171 (2022).
[35]G. Kresse and J. Furthmüller, "Efficient iterative schemes for ab initio total-energy calculations using a plane-wave basis set," Phys. Rev. B **54**(16), 11169 (1996).
[36]G. Kresse and J. Furthmüller, "Efficiency of ab-initio total energy calculations for metals and semiconductors using a plane-wave basis set," Comp. Mater. Sci. **6**(1), 15–50 (1996).
[37]G. Kresse and D. Joubert, "From ultrasoft pseudopotentials to the projector augmented-wave method," Phys. Rev. B **59**(3), 1758 (1999).
[38]J. Hafner, "Ab-initio simulations of materials using VASP: Density-functional theory and beyond," J. Comput. Chem. **29**(13), 2044–2078 (2008).
[39]A. Blanchet, V. Recoules, F. Soubiran, and M. Tacu, "Computation of transport properties of warm dense matter using Abinit," Phys. Plasmas (submitted (2024).
[40]A. H. Romero, D. C. Allan, B. Amadon, G. Antonius, T. Applencourt, L. Baguet, J. Bieder, F. Bottin, J. Bouchet, E. Bousquet, F. Bruneval, G. Brunin, D. Caliste, M. Côté, J. Denier, C. Dreyer, P. Ghosez, M. Giantomassi, Y. Gillet, O. Gingras, D. R. Hamann, G. Hautier, F. Jollet, G. Jomard, A. Martin, H. P. C. Miranda, F. Naccarato, G. Petretto, N. A. Pike, V. Planes, S. Prokhorenko, T. Rangel, F. Ricci, G.-M. Rignanese, M. Royo, M. Stengel, M. Torrent, M. J. van Setten, B. Van Troeye, M. J. Verstraete, J. Wiktor, J. W. Zwanziger, and X. Gonze, "ABINIT: Overview and focus on selected capabilities," J. Chem. Phys. **152**(12), 124102 (2020).
[41]X. Gonze, B. Amadon, G. Antonius, F. Arnardi, L. Baguet, J.-M. Beuken, J. Bieder, F. Bottin, J. Bouchet, E. Bousquet, N. Brouwer, F. Bruneval, G. Brunin, T. Cavignac, J.-B. Charraud, W. Chen, M. Côté, S. Cottenier, J. Denier, G. Geneste, P. Ghosez, M. Giantomassi, Y. Gillet, O. Gingras, D. R. Hamann, G. Hautier, X. He, N. Helbig, N. Holzwarth, Y. Jia, F. Jollet, W. Lafargue-Dit-Hauret, K. Lejaeghere, M. A. L. Marques, A. Martin, C. Martins, H. P. C. Miranda, F. Naccarato, K. Persson, G. Petretto, V. Planes, Y. Pouillon, S. Prokhorenko, F. Ricci, G.-M. Rignanese, A. H. Romero, M. M. Schmitt, M. Torrent, M. J. van Setten, B. Van Troeye, M. J. Verstraete, G. Zérah, and J. W. Zwanziger, "ABINIT project: Impact, environment recent developments," Comput. Phys. Commun. **248**, 107042 (2020).
[42]A. Blanchet, J. Clérouin, M. Torrent, and F. Soubiran, "Extended first-principles molecular dynamics model for high temperature simulations in the ABINIT code: Application to warm dense aluminum," Comput. Phys. Commun. **271**, 108215 (2022).
[43]V. Sharma, L. A. Collins, and A. J. White, "Stochastic and mixed density functional theory within the projector augmented wave formalism for the simulation of warm dense matter," arXiv:2301.12018 (2023).
[44]Q. Xu, A. Sharma, B. Comer, H. Huang, E. Chow, A. J. Medford, J. E. Pask, and P. Suryanarayana, "SPARC: Simulation package for ab-initio real-space calculations," SoftwareX **15**, 100709 (2021).
[45]P. Suryanarayana, P. P. Pratapa, A. Sharma, and J. E. Pask, "SQDFT: Spectral quadrature method for large-scale parallel O(N) Kohn-Sham calculations at high temperature," Comput. Phys. Commun. **224**, 288–298 (2018).
[46]S. Kumar, X. Jing, J. E. Pask, A. J. Medford, and P. Suryanarayana, "Kohn-Sham accuracy from orbital-free density functional theory via Δ-machine learning," J. Chem. Phys. **159**(24), 244106 (2023).
[47]S. Kumar, X. Jing, J. E. Pask, and P. Suryanarayana, "On-the-fly machine learned force fields for the study of warm dense matter: Application to diffusion and viscosity of CH," Phys. Plasmas **31**(4), 043905 (2024).
[48]A. D. Baczewski, L. Shulenburger, M. P. Desjarlais, and R. J. Magyar, *Numerical Implementation of Time-dependent Density Functional Theory for Extended Systems in Extreme Environments* (Sandia National Laboratory, Albuquerque, NM, 2014).
[49]R. J. Magyar, L. Shulenburger, and A. D. Baczewski, "Stopping of deuterium in warm dense deuterium from Ehrenfest time-dependent density functional theory," Contrib. Plasma Phys. **56**(5), 459–466 (2016).
[50]Y. T. Lee and R. M. More, "An electron conductivity model for dense plasmas," Phys. Fluids **27**(5), 1273–1286 (1984).
[51]R. M. More, "Pressure ionization, resonances, and the continuity of bound and free states," in *Advances in Atomic and Molecular Physics*, edited by D. R. Bates and B. Bederson (Academic Press, 1985), Vol. 21, pp. 305–56.
[52]H. Ohta and S. Hamaguchi, "Molecular dynamics evaluation of self-diffusion in Yukawa systems," Phys. Plasmas **7**(11), 4506–4514 (2000).
[53]T. Saigo and S. Hamaguchi, "Shear viscosity of strongly coupled Yukawa systems," Phys. Plasmas **9**(4), 1210–1216 (2002).
[54]L. J. Stanek and M. S. Murillo, "Analytic models for interdiffusion in dense plasma mixtures," Phys. Plasmas **28**(7), 072302 (2021).
[55]Z. Donkó and P. Hartmann, "Thermal conductivity of strongly coupled Yukawa liquids," Phys. Rev. E **69**(1), 016405 (2004).
[56]M. S. Murillo, J. Weisheit, S. B. Hansen, and M. W. C. Dharma-Wardana, "Partial ionization in dense plasmas: Comparisons among average-atom density functional models," Phys. review E **87**(6), 063113 (2013).
[57]L. J. Stanek, R. C. Clay III, M. W. C. Dharma-wardana, M. A. Wood, K. R. C. Beckwith, and M. S. Murillo, "Efficacy of the radial pair potential approximation for molecular dynamics simulations of dense plasmas," Phys. Plasmas **28**(3), 032706 (2021).
[58]H. Yukawa, "On the interaction of elementary particles. I," Proc. Physico-Math. Soc. Jpn. 3rd Ser. **17**, 48–57 (1935).
[59]M. W. C. Dharma-Wardana, L. J. Stanek, and M. S. Murillo, "Yukawa-Friedel-tail pair potentials for warm dense matter applications," Phys. Rev. E **106**(6), 065208 (2022).
[60]M. W. C. Dharma-Wardana and F. Perrot, "Density-functional theory of hydrogen plasmas," Phys. Rev. A **26**(4), 2096 (1982).
[61]G. Faussurier, C. Blancard, and E. Berthier, "Nonlocal thermodynamic equilibrium self-consistent average-atom model for plasma physics," Phys. Rev. E **63**(2), 026401 (2001).
[62]D. A. Liberman, "Self-consistent field model for condensed matter," Phys. Rev. B **20**, 4981–4989 (1979).
[63]C. E. Starrett and D. Saumon, "A simple method for determining the ionic structure of warm dense matter," High Energy Density Phys. **10**, 35–42 (2014).
[64]J. M. Ziman, "A theory of the electrical properties of liquid metals. I: The monovalent metals," Philos. Mag. (1798–1977) **6**(68), 1013–1034 (1961).
[65]D. J. Burrill, D. V. Feinblum, M. R. J. Charest, and C. E. Starrett, "Comparison of electron transport calculations in warm dense matter using the Ziman formula," High Energy Density Phys. **19**, 1–10 (2016).
[66]D. Marx and J. Hutter, *Ab Initio Molecular Dynamics: Basic Theory and Advanced Methods* (Cambridge University Press, 2009).
[67]A. Schleife, Y. Kanai, and A. A. Correa, "Accurate atomistic first-principles calculations of electronic stopping," Phys. Rev. B **91**(1), 014306 (2015).
[68]A. D. Baczewski, L. Shulenburger, M. P. Desjarlais, S. B. Hansen, and R. J. Magyar, "X-ray thomson scattering in warm dense matter without the Chihara decomposition," Phys. Rev. Lett. **116**, 115004 (2016).
[69]Y. H. Ding, A. J. White, S. X. Hu, O. Certik, and L. A. Collins, "Ab initio studies on the stopping power of warm dense matter with time-dependent orbital-free density functional theory," Phys. Rev. Lett. **121**, 145001 (2018).
[70]A. J. White, O. Certik, Y. H. Ding, S. X. Hu, and L. A. Collins, "Time-dependent orbital-free density functional theory for electronic stopping power: Comparison to the Mermin-Kohn-Sham theory at high temperatures," Phys. Rev. B **98**, 144302 (2018).
[71]X. Andrade, C. D. Pemmaraju, A. Kartsev, J. Xiao, A. Lindenberg, S. Rajpurohit, L. Z. Tan, T. Ogitsu, and A. A. Correa, "INQ, a modern GPU-accelerated computational framework for (time-dependent) density functional theory," J. Chem. Theory Comput. **17**, 7447 (2021).
[72]A. J. White, L. A. Collins, K. Nichols, and S. X. Hu, "Mixed stochastic-deterministic time-dependent density functional theory: Application to stopping power of warm dense carbon," J. Phys.: Condens. Matter **34**(17), 174001 (2022).
[73]A. Kononov, T. W. Hentschel, S. B. Hansen, and A. D. Baczewski, "Trajectory sampling and finite-size effects in first-principles stopping power calculations," npj Comput. Mater. **9**(1), 205 (2023).

[74]K. A. Nichols, S. X. Hu, A. White, V. Goncharov, D. I. Mihaylov, L. A. Collins, N. Shaffer, and V. Karasiev, "Time dependent density-functional-theory calculations of the nonlocal electron stopping range for inertial confinement fusion applications," Phys. Rev. E **108**, 035206 (2023).
[75]M. A. L. Marques, N. T. Maitra, F. M. S. Nogueira, E. K. U. Gross, and A. Rubio, *Fundamentals of Time-Dependent Density Functional Theory* (Springer, 2012), Vol. 837.
[76]R. Kubo, "Statistical-mechanical theory of irreversible processes. I. General theory and simple applications to magnetic and conduction problems," J. Phys. Soc. Jpn. **12**(6), 570–586 (1957).
[77]D. A. Greenwood, "The Boltzmann equation in the theory of electrical conduction in metals," Proc. Phys. Soc. **71**(4), 585 (1958).
[78]J. Simoni and J. Daligault, "First-principles determination of electron-ion couplings in the warm dense matter regime," Phys. Rev. Lett. **122**(20), 205001 (2019).
[79]J. Daligault and J. Simoni, "Theory of the electron-ion temperature relaxation rate spanning the hot solid metals and plasma phases," Phys. Rev. E **100**(4), 043201 (2019).
[80]X. Andrade, S. Hamel, and A. A. Correa, "Negative differential conductivity in liquid aluminum from real-time quantum simulations," Eur. Phys. J. B **91**, 229 (2018).
[81]K. Ramakrishna, M. Lokamani, A. Baczewski, J. Vorberger, and A. Cangi, "Electrical conductivity of iron in Earth's core from microscopic Ohm's law," Phys. Rev. B **107**(11), 115131 (2023).
[82]A. A. Correa, "Calculating electronic stopping power in materials from first principles," Comput. Mater. Sci. **150**, 291–303 (2018).
[83]J. P. Perdew, A. Ruzsinszky, J. Tao, V. N. Staroverov, G. E. Scuseria, and G. I. Csonka, "Prescription for the design and selection of density functional approximations: More constraint satisfaction with fewer fits," J. Chem. Phys. **123**(6), 062201 (2005).
[84]Y. Cytter, E. Rabani, D. Neuhauser, and R. Baer, "Stochastic density functional theory at finite temperatures," Phys. Rev. B **97**(11), 115207 (2018).
[85]J. E. Moussa and A. D. Baczewski, "Assessment of localized and randomized algorithms for electronic structure," Electron. Struct. **1**(3), 033001 (2019).
[86]A. J. White and L. A. Collins, "Fast and universal Kohn-Sham density functional theory algorithm for warm dense matter to hot dense plasma," Phys. Rev. Lett. **125**(5), 055002 (2020).
[87]L. Onsager, "Reciprocal relations in irreversible processes. I," Phys. Rev. **37**(4), 405 (1931).
[88]S. R. De Groot and P. Mazur, *Non-Equilibrium Thermodynamics* (Courier Corporation, 2013).
[89]R. Soto, *Kinetic Theory and Transport Phenomena* (Oxford University Press, 2016), Vol. 25.
[90]C. E. Starrett, "Potential of mean force for electrical conductivity of dense plasmas," High Energy Density Phys. **25**, 8–14 (2017).
[91]N. R. Shaffer and C. E. Starrett, "Correlations between conduction electrons in dense plasmas," Phys. Rev. E **101**(1), 013208 (2020).
[92]R. L. Liboff, "Transport coefficients determined using the shielded Coulomb potential," Phys. Fluids **2**(1), 40–46 (1959).
[93]S. Chapman and T. G. Cowling, *The Mathematical Theory of Non-Uniform Gases: An account of the Kinetic Theory of Viscosity, Thermal Conduction and Diffusion in Gases* (Cambridge University Press, 1990).
[94]G. V. Chester and A. Thellung, "The law of Wiedemann and Franz," Proc. Phys. Soc. **77**(5), 1005 (1961).
[95]B. Holst, M. French, and R. Redmer, "Electronic transport coefficients from ab initio simulations and application to dense liquid hydrogen," Phys. Rev. B **83**(23), 235120 (2011).
[96]M. French, G. Röpke, M. Schörner, M. Bethkenhagen, M. P. Desjarlais, and R. Redmer, "Electronic transport coefficients from density functional theory across the plasma plane," Phys. Rev. E **105**(6), 065204 (2022).
[97]C. A. Melton, R. C. Clay III, K. R. Cochrane, A. Dumi, T. A. Gardiner, M. K. Lentz, and J. P. Townsend, "Transport coefficients of warm dense matter from Kohn-Sham density functional theory," Phys. Plasmas **31**(4), 043903 (2024).
[98]F. Lambert and V. Recoules, "Plastic ablator and hydrodynamic instabilities: A first-principles set of microscopic coefficients," Phys. Rev. E **86**(2), 026405 (2012).
[99]S. X. Hu, L. A. Collins, T. R. Boehly, J. D. Kress, V. N. Goncharov, S. Skupsky *et al.*, "First-principles thermal conductivity of warm-dense deuterium plasmas for inertial confinement fusion applications," Phys. Rev. E **89**(4), 043105 (2014).
[100]S. X. Hu, L. A. Collins, V. N. Goncharov, J. D. Kress, R. L. McCrory, and S. Skupsky, "First-principles investigations on ionization and thermal conductivity of polystyrene for inertial confinement fusion applications," Phys. Plasmas **23**(4), 042704 (2016).
[101]S. Jiang, O. L. Landen, H. D. Whitley, S. Hamel, R. London, D. S. Clark, P. Sterne, S. B. Hansen, S. X. Hu, G. W. Collins, and Y. Ping, "Thermal transport in warm dense matter revealed by refraction-enhanced x-ray radiography with a deep-neural-network analysis," Commun. Phys. **6**(1), 98 (2023).
[102]S. X. Hu *et al.*, "A review on charged-particle transport modeling for laser direct-drive fusion," Phys. Plasmas **31**(4), 040501 (2024).
[103]H. M. Milchberg, R. R. Freeman, S. C. Davey, and R. M. More, "Resistivity of a simple metal from room temperature to 10^6 K," Phys. Rev. Lett **61**, 2364–2367 (1988).
[104]A. W. DeSilva and A. D. Rakhel, "Progress in measurements of the electrical conductivity of metal plasmas," Contrib. Plasma Phys. **45**(3–4), 236–242 (2005).
[105]J. Clérouin, P. Noiret, P. Blottiau, V. Recoules, B. Siberchicot, P. Renaudin, C. Blancard, G. Faussurier, B. Holst, and C. E. Starrett, "A database for equations of state and resistivities measurements in the warm dense matter regime," Phys. Plasmas **19**(8), 082702 (2012).
[106]K. R. Cochrane, R. W. Lemke, Z. Riford, and J. H. Carpenter, "Magnetically launched flyer plate technique for probing electrical conductivity of compressed copper," J. Appl. Phys. **119**(10), 105902 (2016).
[107]A. Porwitzky, K. R. Cochrane, and B. Stoltzfus, "Determining the electrical conductivity of metals using the 2 MA Thor pulsed power driver," Rev. Sci. Instrum. **92**(5), 053551 (2021).
[108]K. Widmann, T. Ao, M. E. Foord, D. F. Price, A. D. Ellis, P. T. Springer, and A. Ng, "Single-state measurement of electrical conductivity of warm dense gold," Phys. Rev. Lett. **92**, 125002 (2004).
[109]P. Sperling, E. J. Gamboa, H. J. Lee, H. K. Chung, E. Galtier, Y. Omarbakiyeva, H. Reinholz, G. Röpke, U. Zastrau, J. Hastings, L. B. Fletcher, and S. H. Glenzer, "Free-electron x-ray laser measurements of collisional-damped plasmons in isochorically heated warm dense matter," Phys. Rev. Lett. **115**, 115001 (2015).
[110]Z. Chen, C. B. Curry, R. Zhang, F. Treffert, N. Stojanovic, S. Toleikis, R. Pan, M. Gauthier, E. Zapolnova, L. E. Seipp, A. Weinmann, M. Z. Mo, J. B. Kim, B. B. L. Witte, S. Bajt, S. Usenko, R. Soufli, T. Pardini, S. Hau-Riege, C. Burcklen, J. Schein, R. Redmer, Y. Y. Tsui, B. K. Ofori-Okai, and S. H. Glenzer, "Ultrafast multi-cycle terahertz measurements of the electrical conductivity in strongly excited solids," Nat. Commun. **12**(1), 1638 (2021).
[111]D. Frenkel and B. Smit, *Understanding Molecular Simulation: From Algorithms to Applications* (Elsevier, 2023).
[112]Y. Zhang, A. Otani, and E. J. Maginn, "Reliable viscosity calculation from equilibrium molecular dynamics simulations: A time decomposition method," J. Chem. Theory Comput. **11**(8), 3537–3546 (2015).
[113]T. Q. Qiu and C. L. Tien, "Heat transfer mechanisms during short-pulse laser heating of metals," J. Heat Transfer **115**(4), 835–841 (1993).
[114]W. A. Angermeier, B. S. Scheiner, N. R. Shaffer, and T. G. White, "Disentangling the effects of non-adiabatic interactions upon ion self-diffusion within warm dense hydrogen," Philos. Trans. R. Soc. A **381**(2253), 20230034 (2023).
[115]R. Tucker Sprenkle, L. G. Silvestri, M. S. Murillo, and S. D. Bergeson, "Temperature relaxation in strongly-coupled binary ionic mixtures," Nat. Commun. **13**(1), 15 (2022).
[116]A. Kononov, A. J. White, K. A. Nichols, S. X. Hu, and A. D. Baczewski, "Reproducibility of real-time time-dependent density functional theory calculations of electronic stopping power in warm dense matter," Phys. Plasmas **31**(4), 043904 (2024).
[117]J. Lindhard and A. Winther, "Stopping power of electron gas and equipartition rule," Matemat.-Fysis. Meddel **34**(4), 1–24 (1964).
[118]J. P. Perdew and A. Zunger, "Self-interaction correction to density-functional approximations for many-electron systems," Phys. Rev. B **23**(10), 5048 (1981).

[119]J. P. Perdew, K. Burke, and M. Ernzerhof, "Generalized gradient approximation made simple," Phys. Rev. Lett. **77**(18), 3865 (1996).
[120]V. V. Karasiev, D. I. Mihaylov, and S. X. Hu, "Meta-GGA exchange-correlation free energy density functional to increase the accuracy of warm dense matter simulations," Phys. Rev. B **105**(8), L081109 (2022).
[121]D. I. Mihaylov, V. V. Karasiev, and S. X. Hu, "Thermal hybrid exchange-correlation density functional for improving the description of warm dense matter," Phys. Rev. B **101**(24), 245141 (2020).
[122]N. R. Shaffer, S. X. Hu, V. V. Karasiev, K. A. Nichols, C. E. Starrett, and A. J. White, "Comparing ab initio and quantum-kinetic approaches to electron transport in warm dense matter," Phys. Plasmas (submitted) (2024).